applied sciences

MDPI

Article

Numerical Analysis of Cold Spray Process for Creation of Pin Fin Geometries

Najim Nasire, Mehdi Jadidi * and Ali Dolatabadi

Department of Mechanical and Industrial Engineering, University of Toronto, 5 King's College Rd., Toronto, ON M5S 3G8, Canada; najim.nasire@mail.utoronto.ca (N.N.); ali.dolatabadi@utoronto.ca (A.D.)
* Correspondence: mehdi.jadidi@utoronto.ca

Abstract: A numerical study was performed to analyze the particle deposition of a cold spray process for the preparation of nickel electrocatalysts used in the Hydrogen Evolution Reaction (HER). The study focused on the creation of fin-shaped geometries with an optimal porosity on the electrode surface using a mask located between the nozzle exit and the substrate. Computational Fluid Dynamics (CFD) was performed on a three-dimensional high-pressure nozzle, with nickel powder used as the injection feedstock. The behavior of particles was effectively modeled through a two-way coupled Eulerian–Lagrangian approach. As per the parametric study, four masks of varying wire thicknesses and opening sizes were investigated. The masks were placed at 4 mm increments from the nozzle exit, with the substrate placed at standoff distances (SODs) of 10 mm and 20 mm. To capture the effects of the gas inlet operating conditions, two different nozzle inlet conditions were analyzed (2 MPa and 400 °C, 4 MPa and 800 °C). It was found that the nozzle inlet operating condition had the most significant impact, as it relates to the particle velocity and powder deposition. The high-pressure operating condition resulted in a deposition efficiency (DE) greater than 99.9% for all the test cases, with nearly all the impacted particles depositing on the substrate. For the medium-pressure operating condition, the DE increased linearly as the mask SOD was increased, due to the increase in the particle velocity upon impact.

Keywords: cold spray; computational fluid dynamics; additive manufacturing; hydrogen; electrode

check for updates

Citation: Nasire, N.; Jadidi, M.; Dolatabadi, A. Numerical Analysis of Cold Spray Process for Creation of Pin Fin Geometries. *Appl. Sci.* **2024**, *14*, 11147. https://doi.org/10.3390/app142311147

Academic Editor: Andrea Atrei

Received: 27 October 2024
Revised: 20 November 2024
Accepted: 27 November 2024
Published: 29 November 2024

Copyright: © 2024 by the authors. Licensee MDPI, Basel, Switzerland. This article is an open access article distributed under the terms and conditions of the Creative Commons Attribution (CC BY) license (https://creativecommons.org/licenses/by/4.0/).

1. Introduction

Cold spray is a rapidly growing spraying process that is being extensively adopted in industry due to its favourable properties and wide range of applicability. Compared to other spraying processes, the cold spray process has a high deposition efficiency, high bond strength, and minimal oxidation [1–4]. In the cold spray process, compressed gas (usually nitrogen, helium, or air) is accelerated using a converging–diverging nozzle. Solid powder particles are injected in the nozzle, where they are accelerated to high velocities by momentum exchange with the carrier gas. These high-velocity particles undergo severe plastic deformation upon impact on the substrate surface, allowing for the build up of rapidly depositing material [2–10]. Due to the low temperature of the carrier gas, as well as the short exposure to it, the adhesion of the particles to the substrate is solely due to their kinetic energy during impact [2,3,5,6,11,12]. It is generally accepted that the bonding of these particles to the substrate is achieved when the particle velocity upon impact is greater than a so-called critical velocity [5,11,12]. This critical velocity is dependent on the thermo-mechanical properties of both the particle and substrate and is typically written as a function of the particle temperature and particle diameter [11,12].

Cold spray plays a pivotal role in additive manufacturing and repair [2,3,7,13–15]. A potentially viable use of the cold spray process is for the preparation of electrocatalysts utilized in hydrogen production by water electrolysis [16]. The Hydrogen Evolution Reaction (HER) has been widely studied in recent years as a means of increasing energy

usage from renewable sources. However, it faces major challenges in the efficient hydrogen production required to meet commercial-scale demand [17]. The challenges are associated with the need for stable and low-cost electrocatalysts required for the electrolysis process [17]. Noble-metal-based electrocatalysts, such as platinum-based catalysts, have an excellent catalytic performance for the HER. However, their applicability for commercial use is limited by the scarcity and high costs of the metals [17]. As a result, there have been significant developments in and research on the use of non-noble metals, which have a comparatively lower electrocatalytic performance but are far more abundant and significantly less expensive. To compensate for their lower catalytic activity, several studies have focused on improving their apparent activity by increasing the electrode surface area through the use of surface morphology [16,18,19].

Aghasibeig et al. [16] analyzed the use of nickel powder to coat electrode surfaces using a cold spray process. This experimental study analyzed the electrocatalytic activity of cold-sprayed nickel powder on an aluminum substrate. Three different cold spray operating pressures and temperatures were analyzed. The study found that the cold-sprayed nickel samples outperformed a smooth nickel electrode, having higher electrocatalytic activity. This was due to increases in the active surface area and surface roughness, leading to an increase in the efficiency of the electrolysis process. It was also found that the greatest electrocatalytic activity was obtained for the test case with the lowest deposition efficiency, which also experienced the highest strain accumulation and compressive residual stress. It is believed that this was due to the peening effect, caused by undeposited particles that bounced off the substrate/deposited layer.

Another approach to increasing the electrode surface area and electrocatalytic activity is by creating fin array geometries on the electrode surface. Fin arrays are created by placing a mask (i.e., a wire mesh) in front of the substrate surface. The openings in the mask funnel the particles, allowing for the creation of pyramidal pin fins on the substrate. The use of a mask for the preparation of nickel electrode surfaces has been previously investigated using the High-Velocity Oxy-Fuel spraying process (HVOF) [18], as well as the atmospheric plasma spray and suspension plasma spray process [19]. Both studies found that the electrodes coated using the mask outperformed the electrode deposited without the mask. This increase in electroactivity was attributed to the different roughness levels achieved from the masked spraying processes.

The creation of fin arrays using a mask has also been investigated for the cold spray process. Several studies have analyzed the thermal and hydrodynamic performance of these fin arrays for use in heat exchangers [20–26]. Dupuis et al. [20] experimentally analyzed the heat transfer performance of pyramidal and trapezoidal fin arrays made from a masked cold spray process. Aluminum powder was used as the feedstock and deposited on an aluminum substrate using the masked cold spray process. The study found that the thermal performance of the cold-sprayed fin arrays was substantially better than that of traditional machined rectangular fin arrays of similar characteristic dimensions. This increase in performance was believed to be due to the increase in the convective heat transfer coefficient as a result of the increased turbulence between the rows of fins.

Cormier et al. [21] experimentally analyzed the thermal and hydrodynamic performance of a pyramidal fin array made from a masked cold spray process as well. They analyzed fin arrays made of three different materials (aluminum, nickel, and stainless steel 304), as well as investigated the use of a multi-material fin array to optimize thermal performance for different service temperatures present in heat exchangers. The study found that the generation of the fin arrays created by the masked cold spray process significantly improved the heat transfer performance, due to the increase in the surface roughness of the fins.

The cold spray process is intricate, involving multiple disciplines, including fluid mechanics, solid mechanics, and materials science [2,3,5,6,8–12,14,27–30]. In the present study, numerical simulations are performed to analyze particle deposition, focusing on creating precise fin-like geometries with an optimal porosity on electrode surfaces by

positioning masks between the nozzle and the substrate. Computational Fluid Dynamics (CFD) is employed to simulate the interactions of gas and particles within a high-pressure nozzle, using nickel powder as the feedstock. CFD models are commonly used to optimize nozzle design and predict particle trajectories, velocities, and temperatures in the cold spray process [7,29,31–43]. They offer crucial insights into how process parameters, such as gas pressure and temperature, as well as nozzle design, influence particle velocity and trajectory. These factors directly influence the deposition efficiency and coating quality. In this study, particle in-flight behavior is modeled using a two-way coupled Eulerian–Lagrangian approach, which includes an appropriate drag correlation to account for compressibility and rarefaction effects. A parametric study explores the effects of varying wire thicknesses and opening areas of different masks, inlet pressures and temperatures, standoff distances, and mask positions on the particle conditions upon impact.

2. Numerical Modelling

To model the gas flow and particle in-flight behavior, the Eulerian–Lagrangian approach implemented in ANSYS FLUENT V23.2 was employed. The gas phase was initially solved from a steady-state perspective. Once convergence was achieved, the particles were injected and tracked using the transient Lagrangian solver, the Discrete Phase Model (DPM).

2.1. Geometry and Boundary Conditions

The geometry of the nozzle, mask, and substrate is presented in Figure 1. Due to the presence of the mask, the analysis needed to be modelled in three dimensions. However, the flow and overall particle deposition are symmetric about two planes, therefore, a quarter-symmetric model was utilized. The dimensions of the converging–diverging nozzle are the same as those in the study performed by Garmeh et al. [31] (which was based on a PCS 800 cold spray system (Plasma Giken, Yoriimachi, Japan)) and are shown in Figure 2. Furthermore, Figure 2 identifies the standoff distance (SOD) parameter for both the mask and the nozzle, which was varied in this parametric study.

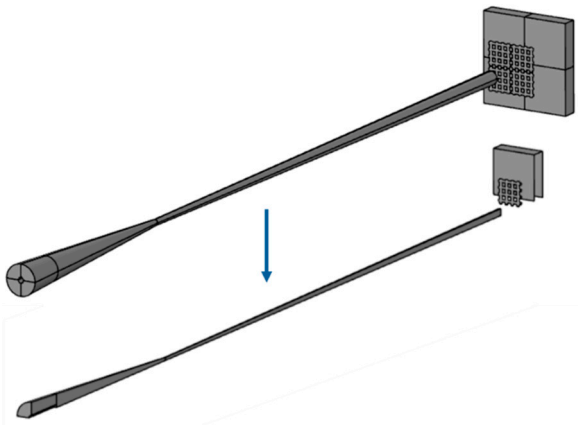


Figure 1. Quarter-symmetric model of nozzle, mask, and substrate.

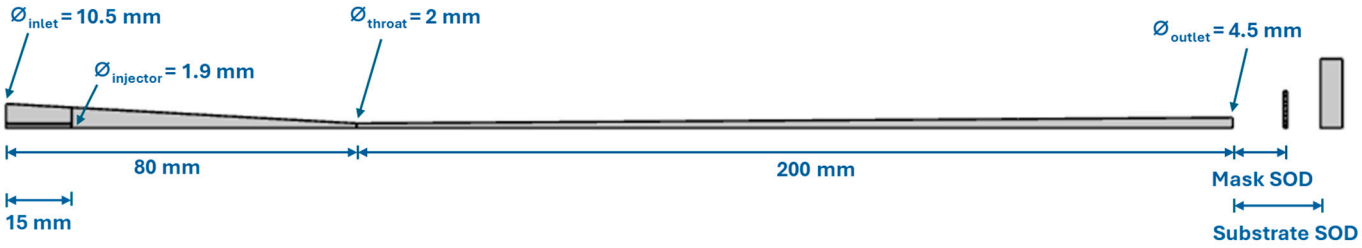


Figure 2. Nozzle dimensions and geometry. SOD stands for standoff distance.

The flow domain is shown in Figure 3. Similar to previous studies [31,32,43,44], the outlet boundary is treated as a pressure outlet, and all the walls (nozzle, mask, and substrate) are treated with no-slip conditions. A pressure inlet is specified at the nozzle inlet. The substrate used for the analysis is a square prism, 30 mm × 30 mm × 5 mm. The jet flows out radially after it impinges on the substrate surface. Therefore, to minimize the effect of the outlet conditions, the domain is extended 80 mm from the nozzle centerline. The domain is also extended to 50 mm behind the substrate surface and 30 mm behind the nozzle exit, since the flow can be reflected off the substrate.

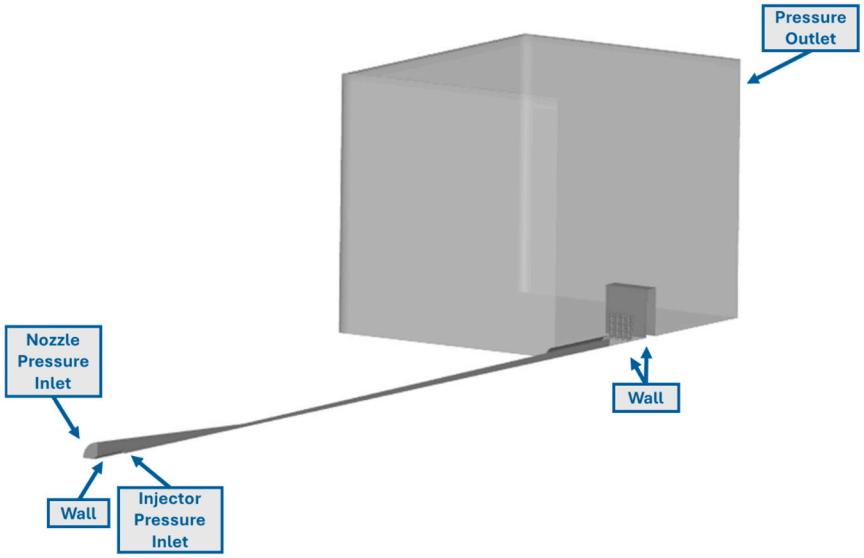


Figure 3. Flow domain and boundary conditions.

2.2. Study Parameters

For the parametric study, four different masks were analyzed. The geometry specifications of the masks are shown in Table 1. The masks were modelled based on dimensions from commercially available products. For the study, two different mask rod diameters were analyzed, a smaller rod diameter and a larger rod diameter. Each mask also had a different opening area. It should be noted that the masks were modelled as a simplified mesh—the overlapping and weaving of the mesh rods were not considered in this analysis. To capture the effect of the substrate SOD, the analysis was performed at the following two substrate SODs: 10 mm and 20 mm. To analyze the effects of the mask SOD, the mask distance from the nozzle exit was increased at increments of 4 mm. The different test configurations and SODs are described in Table 2.

Table 1. Mask properties.

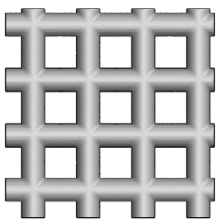
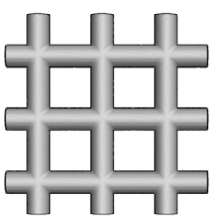
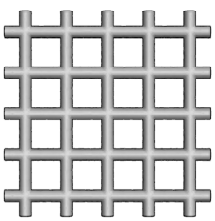
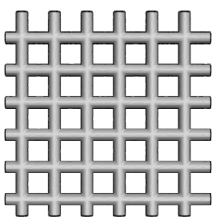
	Mask 1	Mask 2	Mask 3	Mask 4
Wire Diameter (mm)	0.89	0.89	0.46	0.46
Opening Size (mm)	1.22	1.65	1.14	0.81
% Open Area	33	42	51	41
Model				

Table 2. Substrate and mask standoff distances.

	10 mm Substrate SOD (from Nozzle Exit to Substrate)	20 mm Substrate SOD (from Nozzle Exit to Substrate)
Mask SOD (from Nozzle Exit to Mask)	4 mm 8 mm	4 mm 8 mm 12 mm 16 mm

The deposition of particles in a cold spray process is very sensitive to the inlet operating conditions of the nozzle. A higher pressure would allow particles to achieve greater velocities, as a result significantly increasing the chances of deposition. Therefore, to analyze the effect of the nozzle inlet conditions, the following two operating conditions were analyzed: a medium-pressure case and a high-pressure case. See Table 3 for the operating conditions, which are the same as those in the study performed by Garmeh et al. [31]. A total of 48 simulations were performed for the parametric study. The analysis captured the effects of the mask geometry, the substrate SOD, the mask SOD, and the nozzle inlet operating conditions.

Table 3. Nozzle inlet operating conditions.

Case	Inlet Pressure (MPa)	Inlet Temperature (°C)
Medium Pressure	2	400
High Pressure	4	800

2.3. Mesh

The mesh for the analysis was generated using ANSYS Workbench 2023 R2 and is shown in Figure 4 for the entire domain. The mesh was semi-structured and consisted of 1,500,000 to 2,600,000 cells (depending on the mask analyzed and the SODs). The mesh consisted primarily of structured hexahedral cells, located in the nozzle and most of the external domain. Due to the complex geometry of the mask, the mesh around the mask was unstructured and consisted of tetrahedral and prismatic cells. This semi-structured/unstructured mesh can be seen in detail in Figure 5. The mesh sensitivity analysis is described in Appendix A.

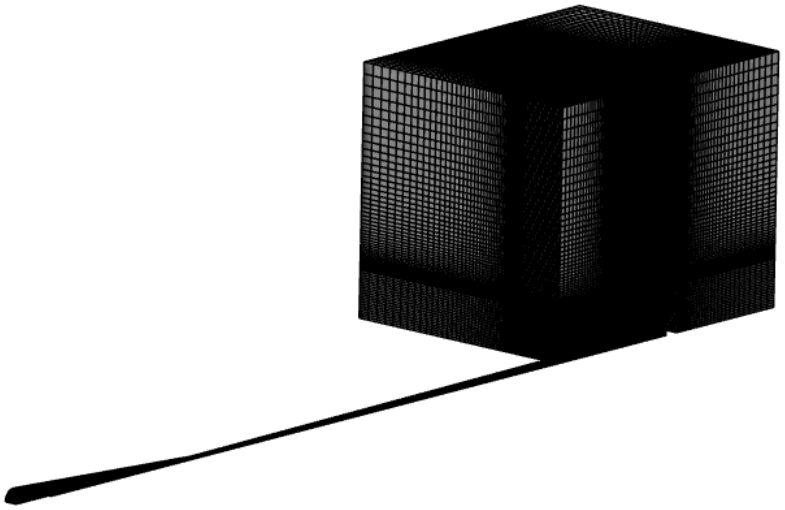


Figure 4. Mesh of the entire domain.

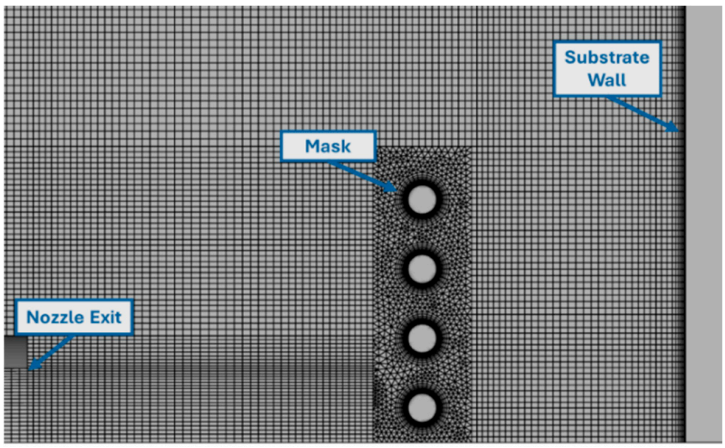


Figure 5. Zoomed-in view of the mesh, showing structured and unstructured regions.

2.4. Continuous Phase

The gas flow was solved using the steady-state pressure-based solver. Nitrogen was used as the operating fluid and modelled using the ideal gas assumption. To account for compressibility and thermal effects, the temperature-dependent three-coefficient Sutherland equation was used to model the fluid viscosity. The temperature-dependent piecewise-polynomial relationship was used to model the specific heat. Second-order schemes were used for spatial discretization. The coupled scheme was implemented for the pressure–velocity coupling, as it resulted in a better convergence behavior. The SST k-ω model was used as the turbulence model for the analysis, with viscous heating enabled. A comparison of the k-ε realizable and SST k-ω models is reported in Appendix B to show that the SST k-ω model was considerably better at analyzing the near-wall behavior of supersonic jets near and downstream of the masks as compared to k-ε models.

2.5. Discrete Phase

The discrete phase (i.e., particles) was solved using the transient Lagrangian Discrete Phase Model (DPM) in FLUENT. As mentioned, the continuous phase was initially fully resolved, at which point, the transient particles were injected. The particle injection time step was set at 10^{-5} s. Two-way turbulence coupling was enabled to account for changes in turbulent quantities. Depending on the size of the particle, particles can dampen or produce turbulent eddies, which is accounted for using turbulence coupling [45]. O'Rourke's stochastic collision [45,46] was also enabled, as it results in a greater dispersed particulate flow, which is closer to experimental observation [31]. Stochastic tracking using the Discrete Random Walk (DRW) model was also enabled, which considers the effects of turbulent velocity fluctuations on the particle trajectories [45].

Nickel powder was used as the particle feedstock. The nickel powder was injected normally to the injector surface at 10 m/s and 300 K, at a mass flow rate of 1 g/s. The injector surface was treated as a pressure inlet, with an inlet pressure 10% higher than the nozzle inlet pressure [31]. The inlet temperature was kept the same as the nozzle inlet temperature. The powder diameter ranged from 17 µm to 77 µm, with a mean diameter of 48 µm. The particle diameter distribution was based on the Rosin–Rammler distribution from the study performed by Garmeh et al. [31].

To better capture the drag behavior of the particles at the high flow speeds, the drag correlation proposed by Crowe was implemented. The Crowe's drag coefficient is valid for a wide range of particle Mach and Reynolds numbers and considers compressibility and rarefaction effects [31,43,47,48]. To model the particle heat transfer, the Ranz–Marshall correlation was used for the calculation of the Nusselt number. The lumped capacity method was used, neglecting the temperature gradient inside the particle. Similar to previous studies [31–33], the trap boundary condition was used at the substrate and mask.

When a particle landed on the substrate surface or the mask, it was assumed to adhere to the surface and was removed from the simulation.

3. Results

The gas pressure, velocity, and temperature contours are shown in the figures below. Figures 6 and 7 show the medium- and high-pressure cases for Mask 2. Figures 8 and 9 show the medium- and high-pressure cases for Mask 4. The medium- and high-pressure cases for Mask 1 and Mask 3 are shown in Appendix C.

In these figures, the first row illustrates the variation in static pressure across different masks and SODs. It is evident that changes in the inlet conditions, mask type, and mask and substrate SODs significantly alter the pressure distribution. The second row depicts the velocity magnitude of the gas flow, while the third row shows the temperature distribution. Similar to the pressure, both the velocity and temperature are greatly influenced by the inlet conditions, the mask type, and the mask and substrate SODs. In general, the typical shock diamond structures seen in cold spray processes [34,43] or the simple bow shock formed near a flat substrate [30–32] are replaced by highly complex supersonic jets when a mask is placed between the nozzle exit and the substrate.

As can be seen, the gas pressure, velocity, and temperature are significantly higher for the higher-pressure cases compared to the medium-pressure cases. Due to the higher inlet pressure and temperature, the flow is accelerated to greater gas velocities. There appears to be a bow shock upstream of the mask, which creates a high-pressure zone, as well as increasing the gas temperature and decreasing the gas velocity. In addition to this, there also appears to be a pressure rise in the stagnation zone at the substrate surface. The reduction in gas velocity due to the mask can potentially decrease the particle velocity and, hence, the deposition efficiency. A study performed by Pattison et al. [30] found that the bow shock caused by small substrate SODs had a significant adverse effect, causing a reduction in the particle impact velocity and deposition efficiency. Therefore, the shock experienced due to the mask could significantly impact the particle deposition, especially for small mask SODs.

The gas pressure and velocity profiles are analyzed along the jet centerline from the nozzle exit to the substrate surface. The gas pressure and velocity profiles for the medium-pressure case are shown in Figures 10 and 11, respectively. Likewise, the gas pressure and velocity profiles for the high-pressure case are shown in Appendix D. The figures show the gas profile along the centerline for each of the four masks, for all the test cases. The mask location and approximate size are overlayed on each plot. The gas temperature profiles along the centerline are presented in Appendix E.

From the profiles, the bow shock that is formed upstream of the mask is evident by the sudden rise in the gas pressure, decrease in the gas velocity, and rise in the gas temperature. Interestingly, the bow shock appears to be of a consistent magnitude for the medium-pressure case. Irrespective of the test case, the pressure rise, velocity decrease, and temperature rise are of a similar size and shape along the centerline where the majority of the particles move. It should be noted that Masks 1 and 2 (red and blue) experience bow shock earlier in the flow due to their larger rod diameters, compared to Masks 3 and 4 which have smaller rod diameter. For the high-pressure case, the magnitude of the bow shock formed upstream of the mask varies based on the mask and mask location. The bow shock also appears to be more severe compared to the medium-pressure case, resulting in a higher gas velocity decrease. The bow shock that is formed in the stagnation zone at the substrate surface is also evident, as indicated by the rise in pressure near the substrate. However, the bow shock at the substrate is of a lesser magnitude compared to that at the mask.

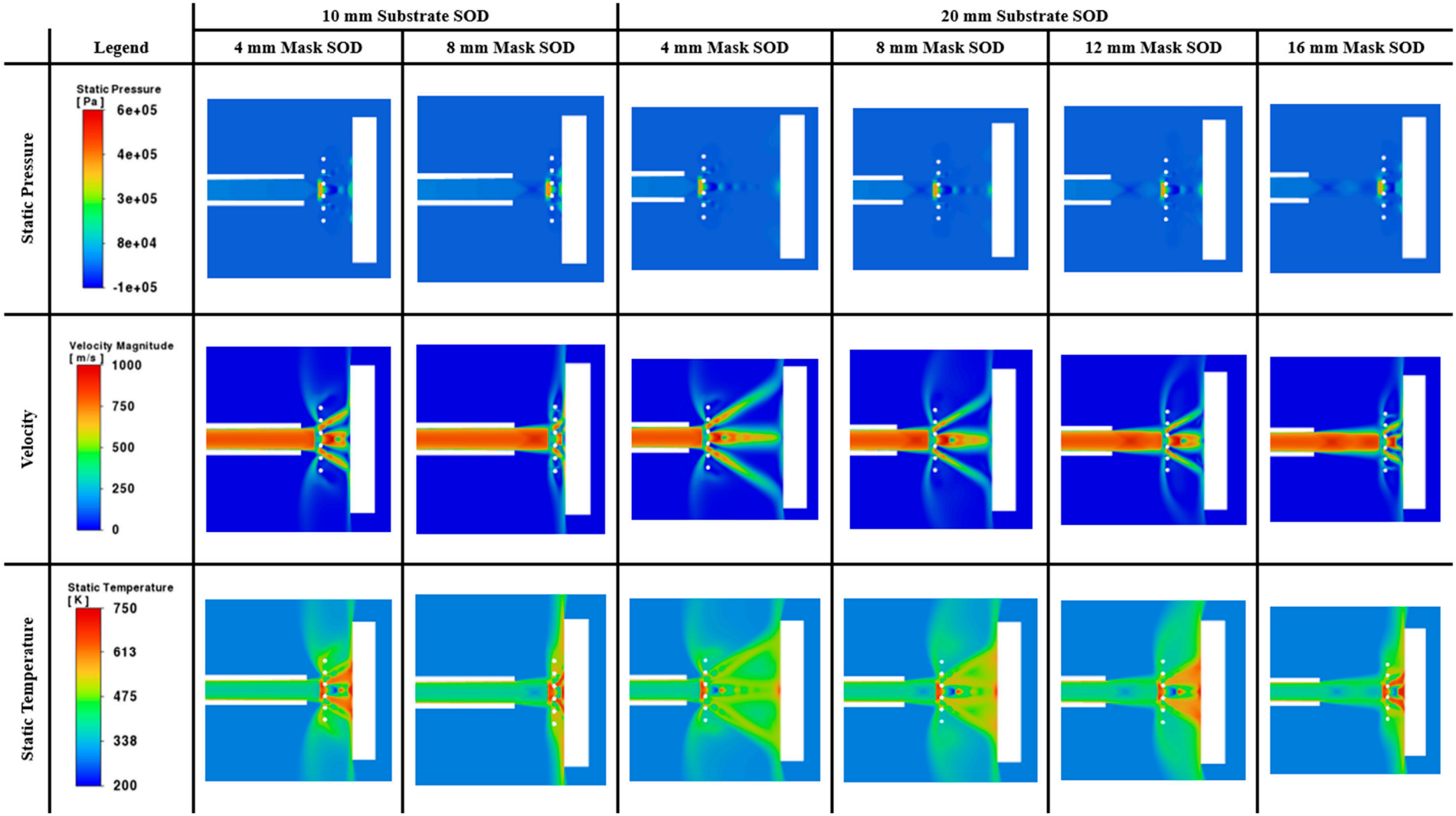


Figure 6. Flow contours for Mask 2 (medium-pressure case).

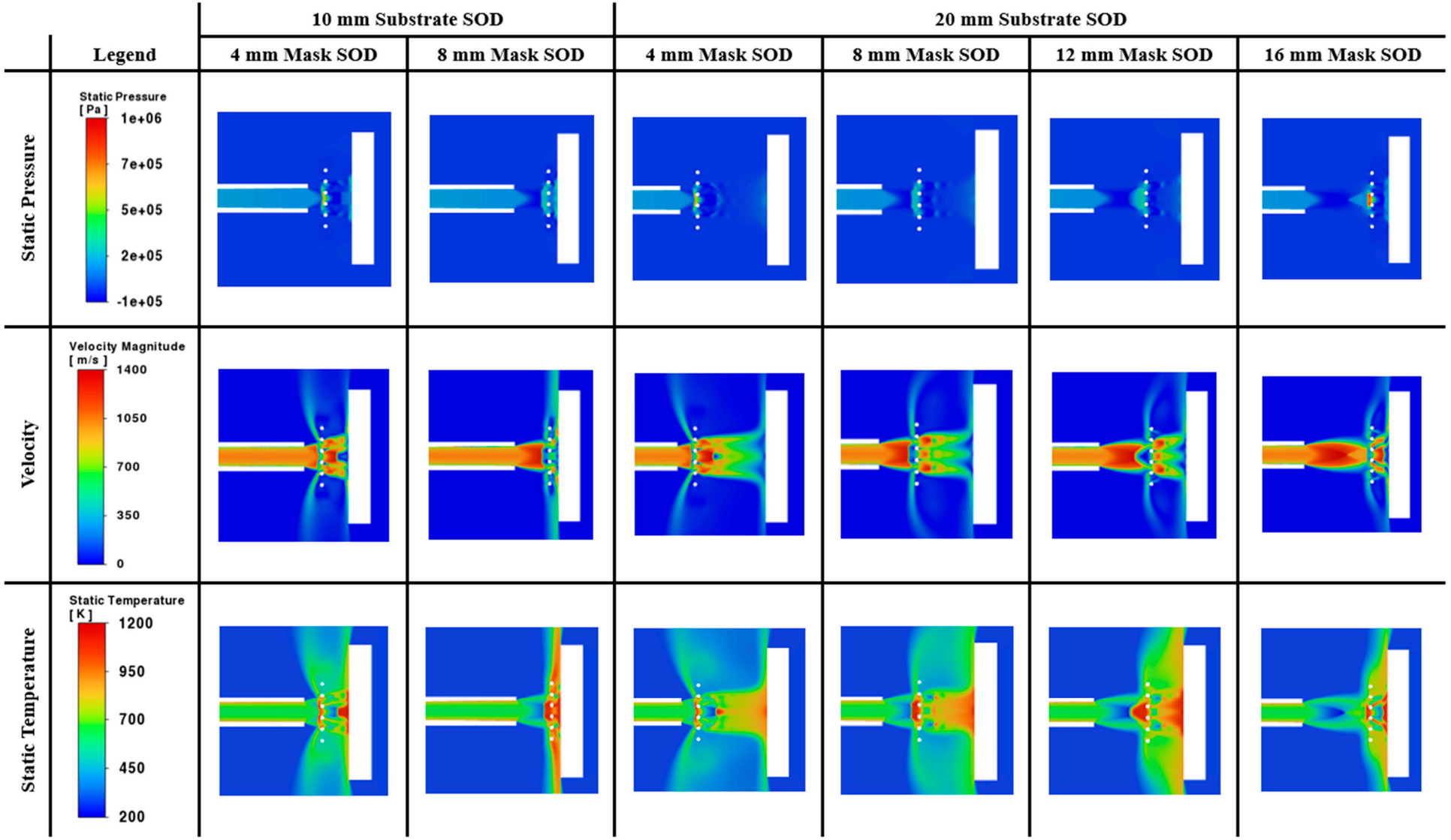


Figure 7. Flow contours for Mask 2 (high-pressure case).

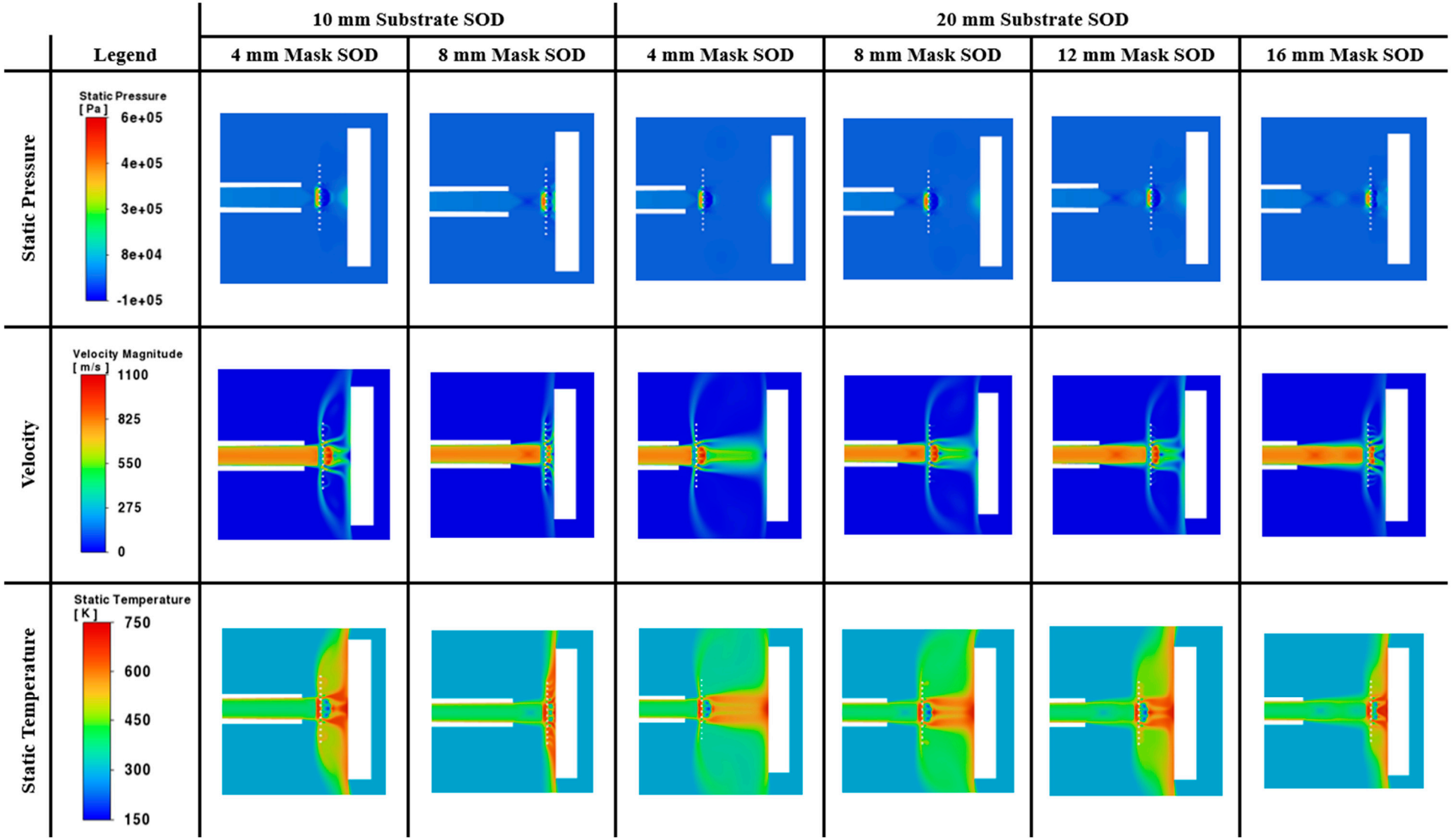


Figure 8. Flow contours for Mask 4 (medium-pressure case).

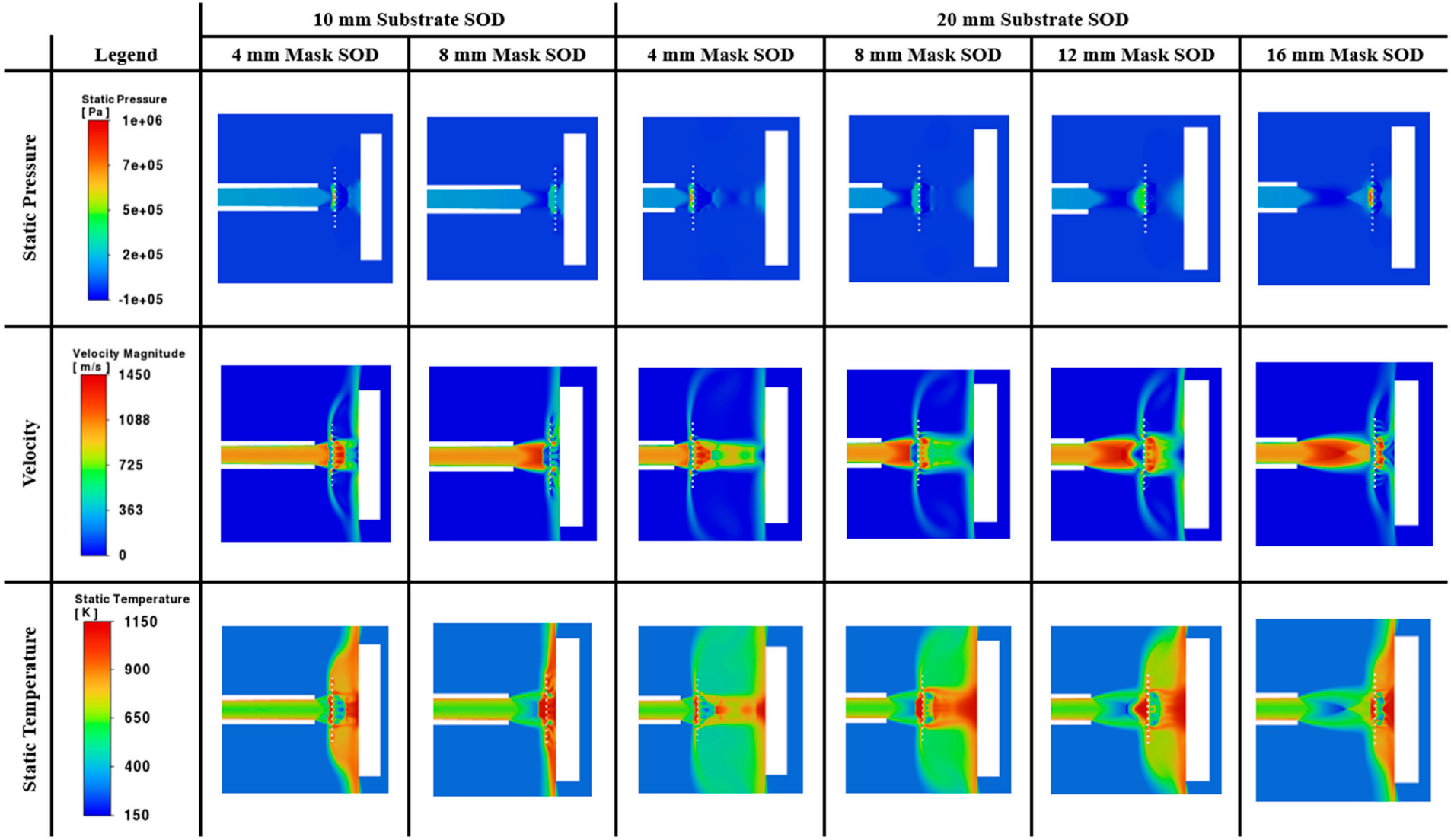


Figure 9. Flow contours for Mask 4 (high-pressure case).

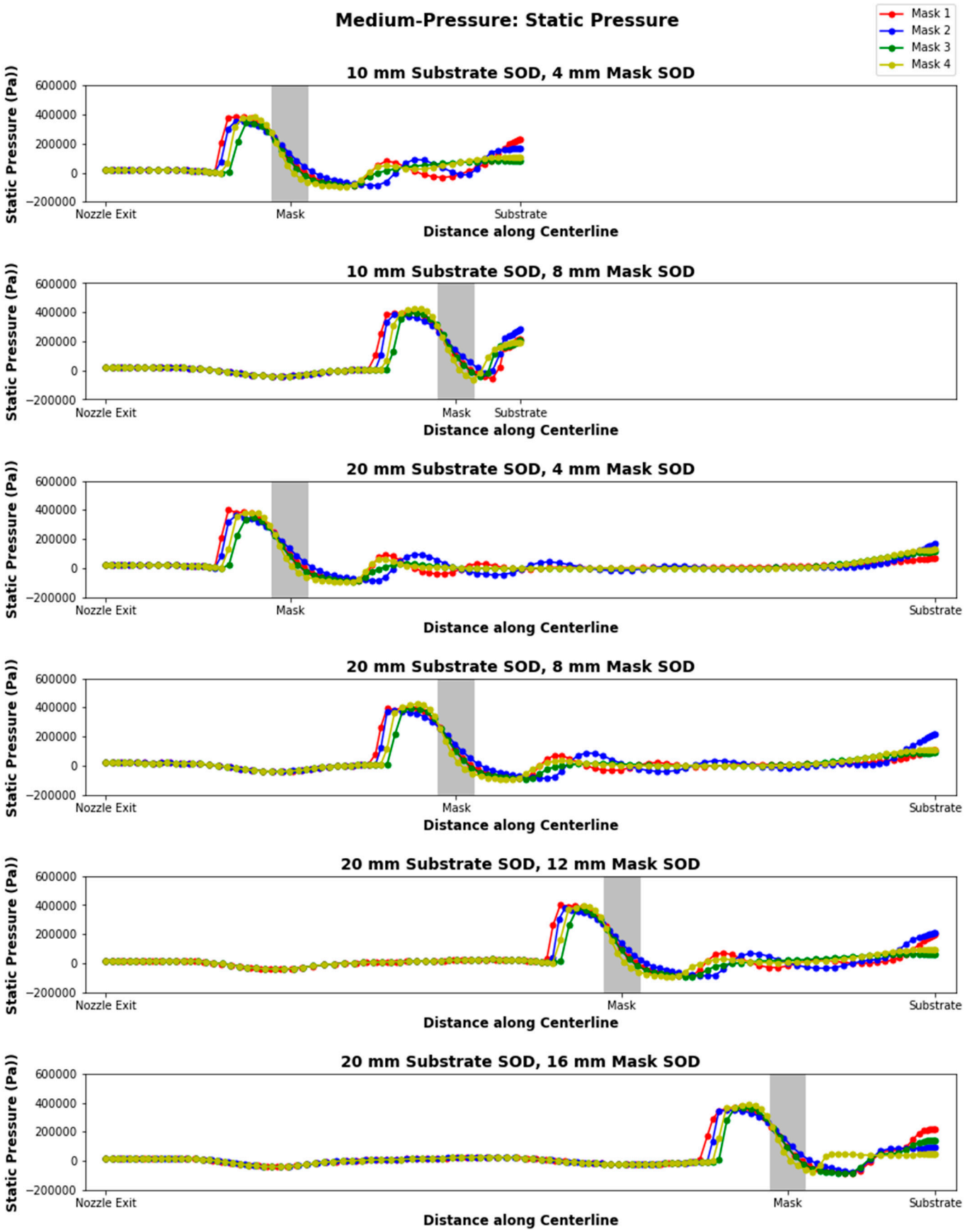


Figure 10. Gas pressure profile along centerline (medium-pressure case).

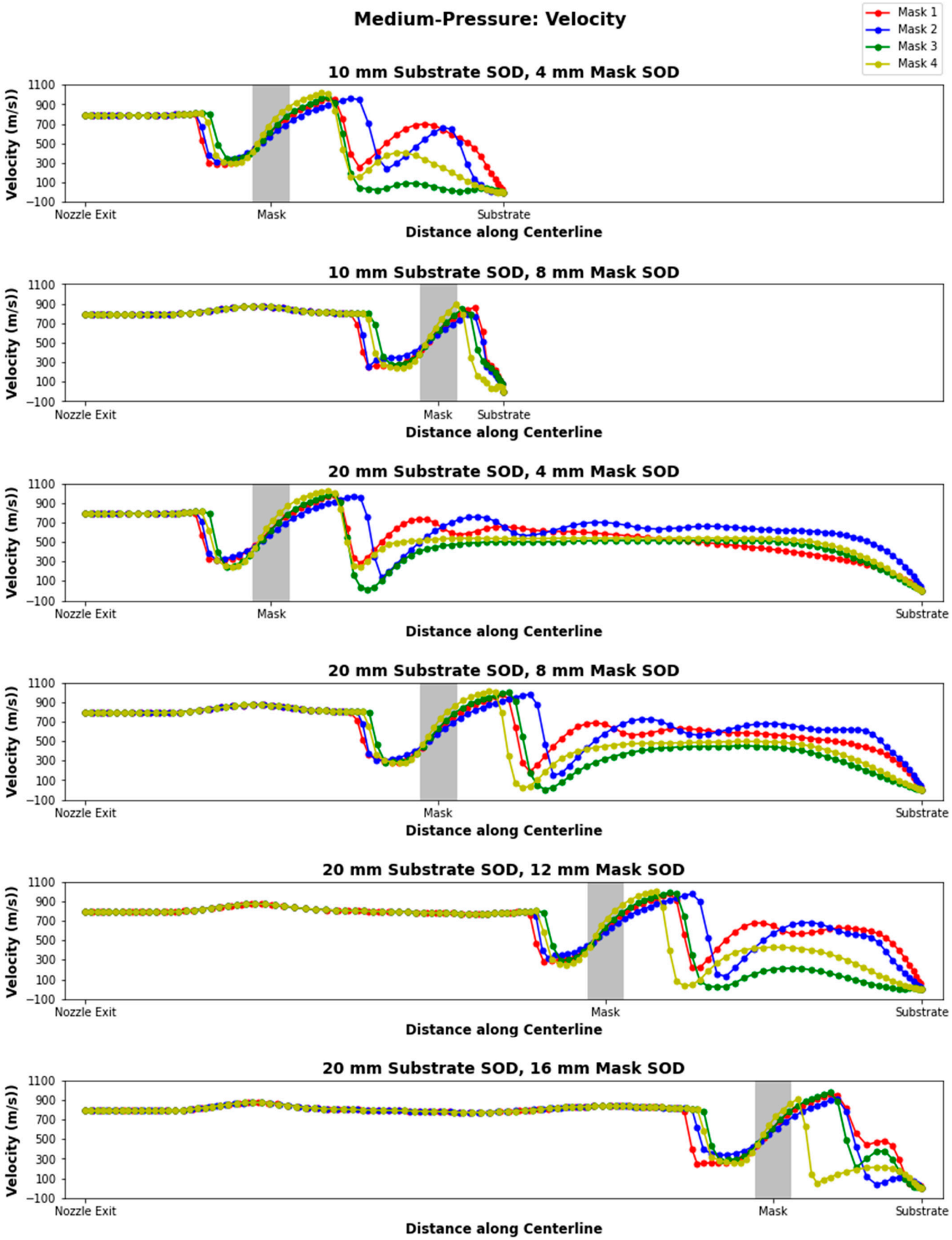


Figure 11. Gas velocity profile along centerline (medium-pressure case).

As the flow enters the mask, the gas velocity along the centerline increases due to the fluid being funneled between the mask rods. The velocity suddenly decreases downstream of the mask, as it passes through another shock—as evidenced by the sudden rise in pressure. It is interesting to note the flow differences experienced by the four different masks. For the medium-pressure case, Masks 1 and 2 (which have larger rod diameters) generally have a higher gas velocity downstream of the mask (prior to the substrate). It is also worth noting that Masks 1 and 2 experience significant oscillations downstream of the mask, whereas Masks 3 and 4 do not.

The particle distribution on the substrate is presented in Figure 12 for the medium-pressure case and Figure 13 for the high-pressure case. The figures show the particles that landed on the substrate for the four different masks, at each SOD analyzed. A comparison of Figures 12 and 13 reveals that the nozzle inlet conditions are the most critical factor influencing the particle velocity. Notably, increasing the inlet pressure leads to a significant rise in the particle velocity. In addition, as can be seen, the particle impact velocity decreases with an increase in the particle size. Moreover, the particle impact velocity generally decreases as the radial distance from the jet centerline (point (0, 0)) increases.

Given the crucial role of particle impact velocity in determining the deposition rate and coating quality, quantitative data on the average particle impact velocity as a function of operating conditions, mask type, and SODs have been compiled. Figures 14 and 15 show the average particle velocities at the nozzle exit and before entering the mask for both the medium- and high-pressure cases. As can be seen, increasing the inlet pressure from 2 to 4 MPa raises the particle impact velocity from approximately 430 to 580 m/s, highlighting the significant influence of inlet pressure on the particle velocity. With a specific inlet pressure, the average velocity of all the particles at the nozzle exit is approximately the same for all test cases. However, the average velocity of all the particles before entering the mask appears to slightly increase as the mask SOD is increased. This trend can be seen for both the medium- and high-pressure cases. The increase in the average particle velocity with mask SOD is most likely due to the particles being able to accelerate for a greater duration. As can be seen from the centerline gas velocity profiles, the presence of the mask impedes the flow, with the gas velocity decreasing upstream of the mask. As the mask is moved further away from the nozzle exit, the particles are allowed to accelerate for a longer period in the high-velocity gas.

The average velocity of all the particles is also compared after exiting the mask and before impacting the substrate. This can be seen in Figures 16 and 17 for the medium- and high-pressure cases, respectively. As demonstrated, an increase in the inlet pressure from 2 to 4 MPa results in a significant rise in the particle impact velocity from approximately 440 m/s to 590 m/s. As previously discussed, this emphasizes that the inlet pressure has a substantial impact on the particle velocity. Mask properties also play a role, with Mask 1 generating the highest velocity for a given inlet pressure. However, for any specific mask, there is minimal to no change in the average particle velocity after exiting the mask. In addition, similar to the trend in Figures 14 and 15, increasing the mask SOD results in a slight increase in the average particle velocity. It is worth mentioning that variations in the average particle temperature with the SODs and mask properties are negligible (see Appendix F). In other words, the main parameters that control the particle impact conditions are the inlet pressure and temperature.

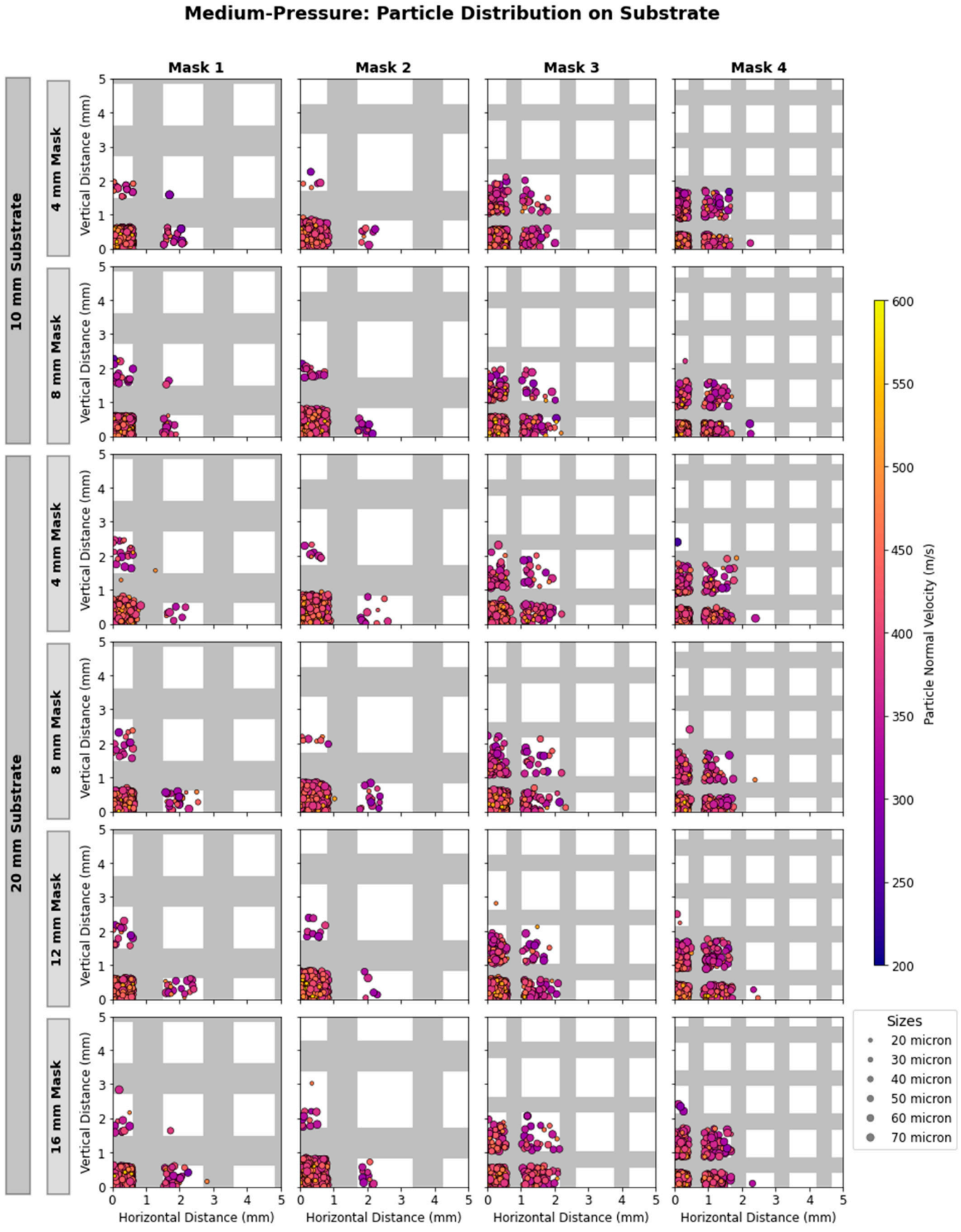


Figure 12. Particle distribution on substrate (medium-pressure case).

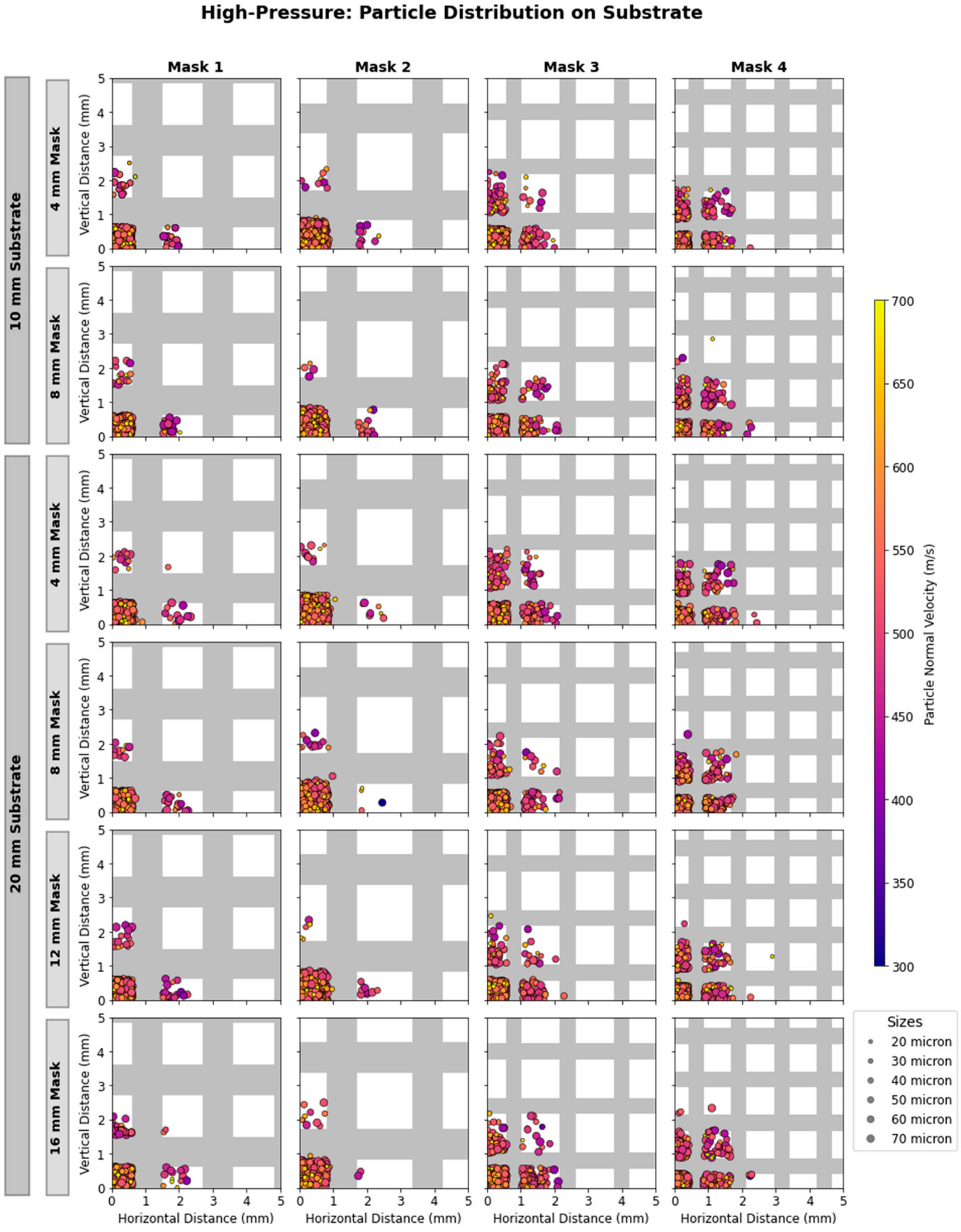


Figure 13. Particle distribution on substrate (high-pressure case).

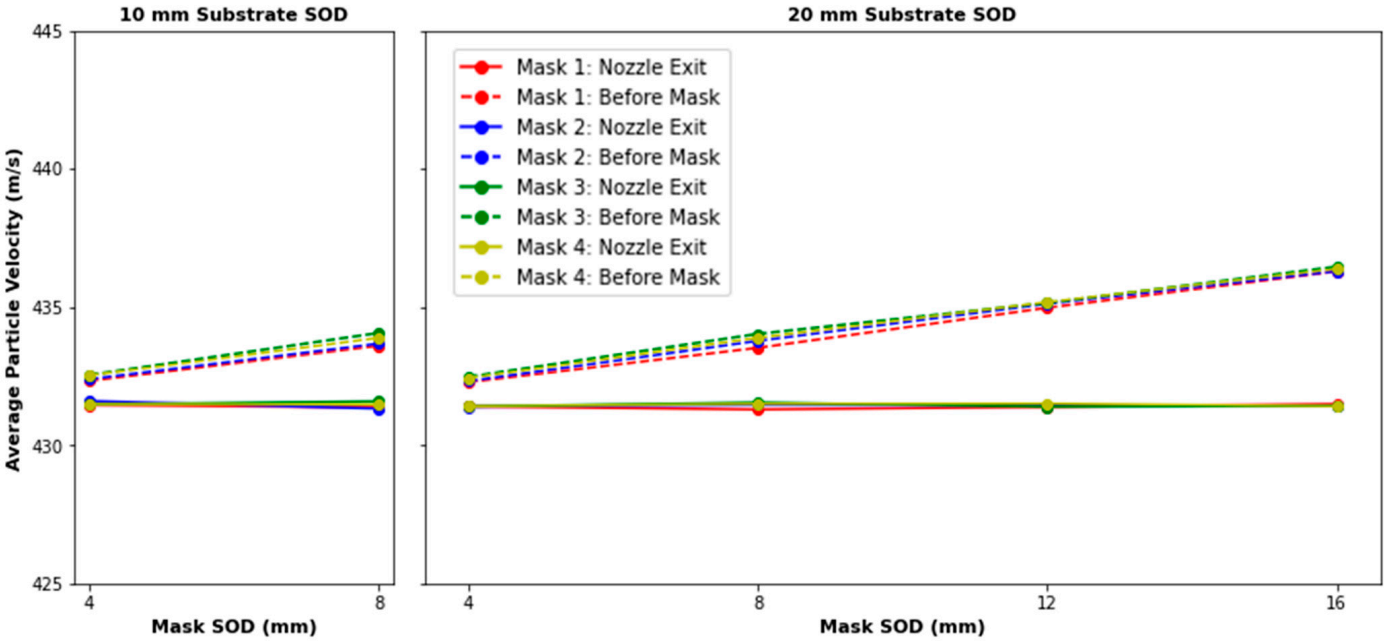


Figure 14. Average particle velocity at nozzle exit and before entering the mask (medium-pressure case).

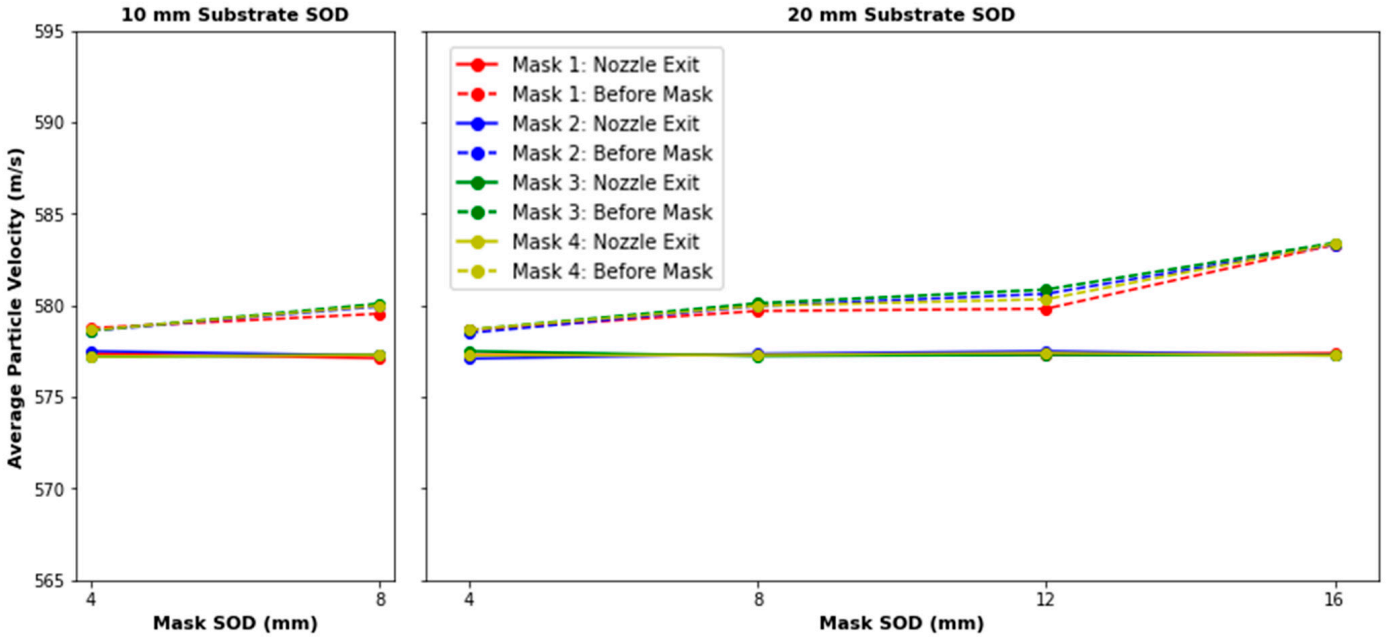


Figure 15. Average particle velocity at nozzle exit and before entering the mask (high-pressure case).

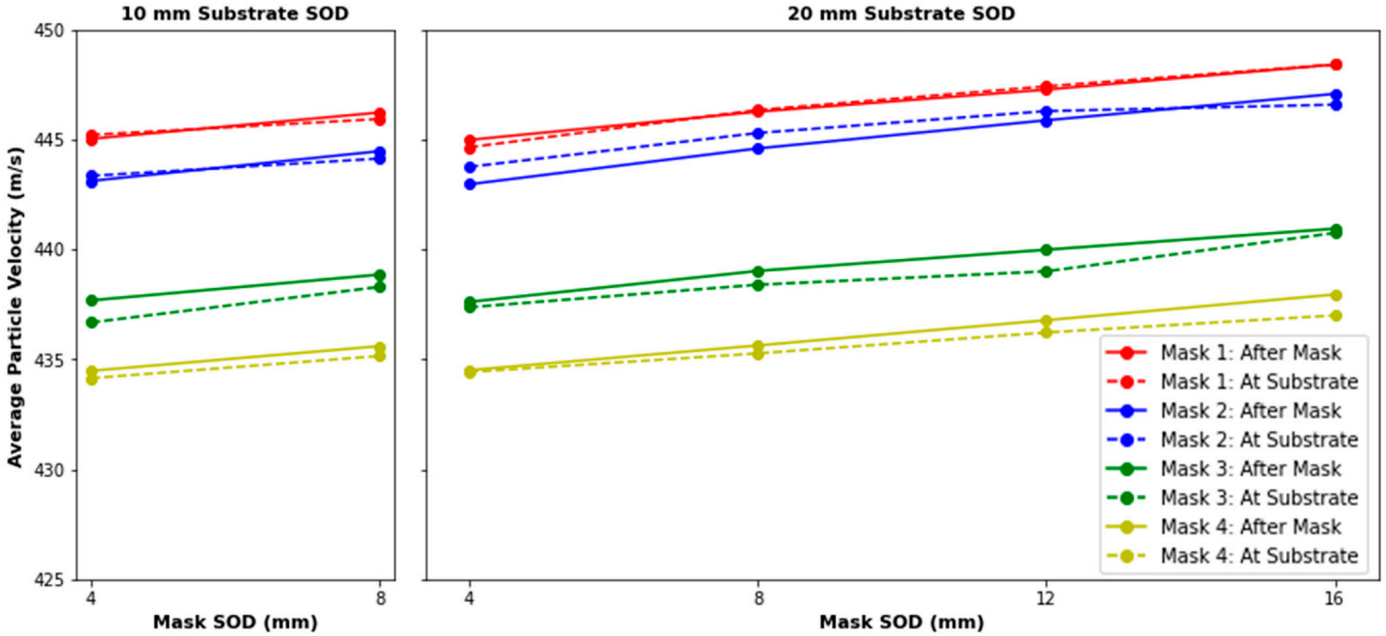


Figure 16. Average particle velocity after exiting mask and before impacting substrate (medium-pressure case).

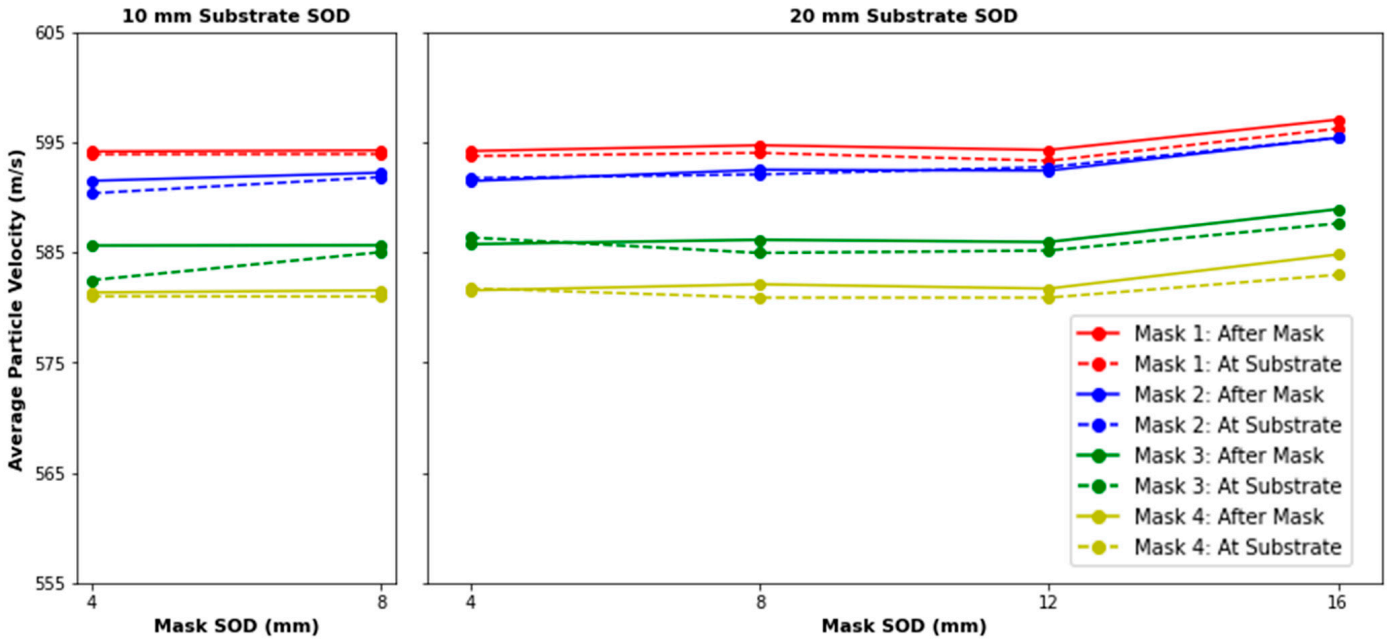


Figure 17. Average particle velocity after exiting mask and before impacting substrate (high-pressure case).

Figure 18 illustrates the particle dispersion and velocity at various locations for the medium-pressure case. In this figure, Mask 1 is used, with a mask SOD of 16 mm and a substrate SOD of 20 mm. The corresponding particle dispersion and velocity for the high-pressure case are provided in Appendix G. The results indicate that minor dispersion occurs before the mask, corresponding to the region where the main shock wave and pressure rise are observed. However, after the mask, no significant particle dispersion is detected. Only very small particles (~20 μm) exhibit slight dispersion under medium-pressure conditions, attributed to their lower Stokes number [49–52].

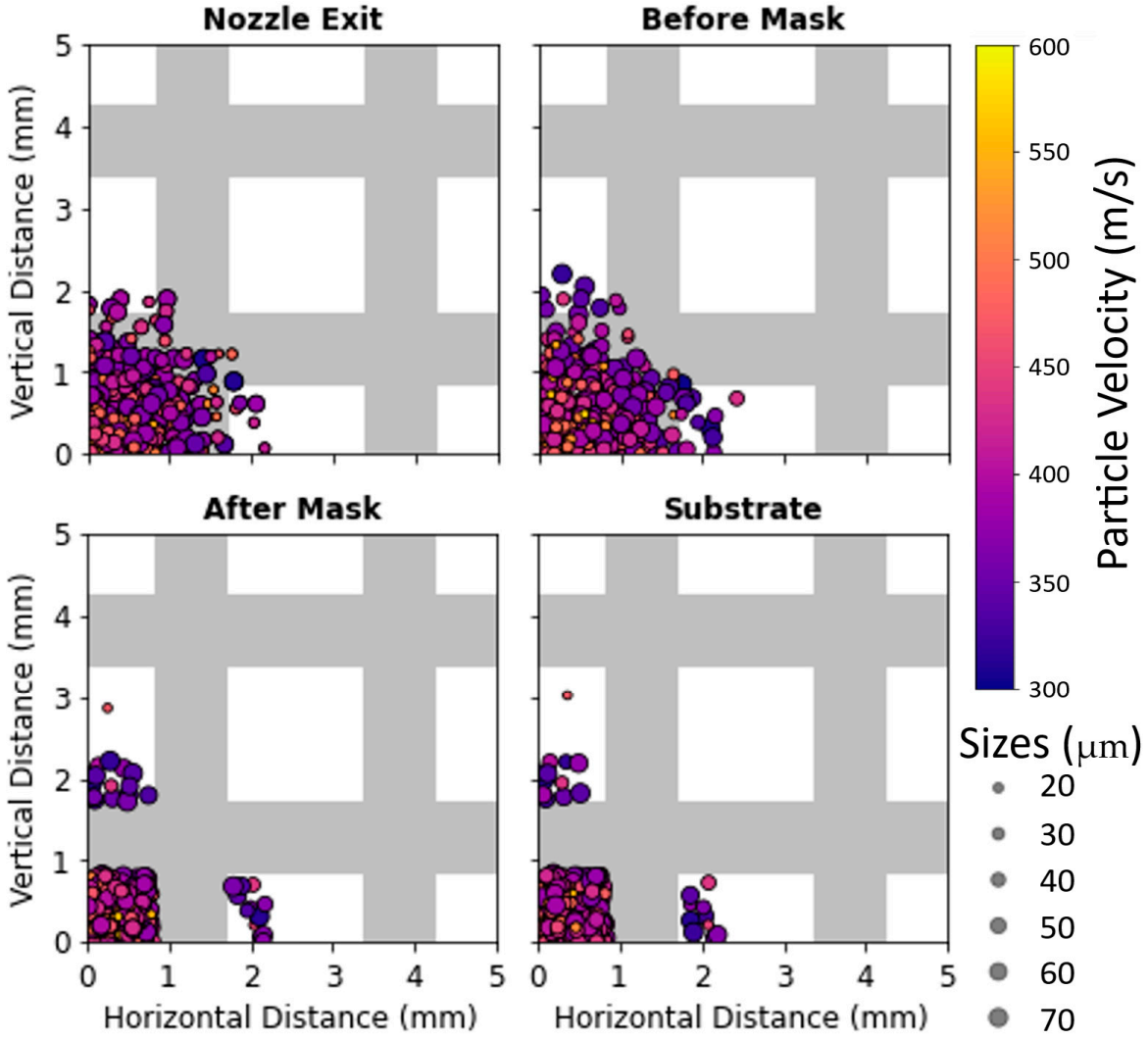


Figure 18. Particle distribution at different locations: Mask 1, 16 mm Mask SOD, 20 mm substrate SOD, medium-pressure case.

To determine whether a particle will adhere to the substrate surface, the particle's impact velocity from numerical simulations must be compared with the critical velocity, either calculated or experimentally measured. If the particle's impact velocity exceeds this critical threshold, it is likely to be deposited on the substrate. Bae et al. [53] utilized Finite Element Analysis (FEA) to estimate the critical impact velocity for nickel powder on a mild steel substrate. To the best of the authors' knowledge, these are the only available critical velocity data for nickel powder that account for the effects of both the particle diameter and temperature. Therefore, we analyze the deposition rate and efficiency by comparing our CFD-simulated particle impact velocities with the critical velocity data from Bae et al. [53]. This comparison is expected to be valuable for readers interested in the topic, and also underscores the need for further research to develop critical velocity correlations for a broader range of powder and substrate materials.

The critical velocity correlation for nickel powder (Equation (1)) is developed in the current study based on the data presented in the work of Bae et al. [53], as follows:

$$\text{Critical Velocity} = \frac{\left(1.025 - \left(5.87 \times 10^{-15}\right) \times {T_p}^{3.88}\right)^{251}}{\left(-0.3 + 26374 \times d_p\right)^{0.34}}, \quad (1)$$

where T_p (K) is the particle temperature upon impact and d_p (m) is the particle diameter.

The fitted critical velocity correlation provides a decent interpolation and extrapolation of the FEM data. The fitted equation is compared with the FEM data [53] and is shown in Figure 19. Since Bae et al.'s study analyzed nickel particles ranging from 25 to 75 μm, the data needed to be extrapolated for this study to include the present particle diameter range (from 17 to 77 μm). The curve fitted Equation (1) has an R^2 of 0.964 with respect to the original study data [53]. As mentioned, if the particle velocity upon impact on the substrate is greater than the critical velocity, it is assumed that the particle deposits on the substrate.

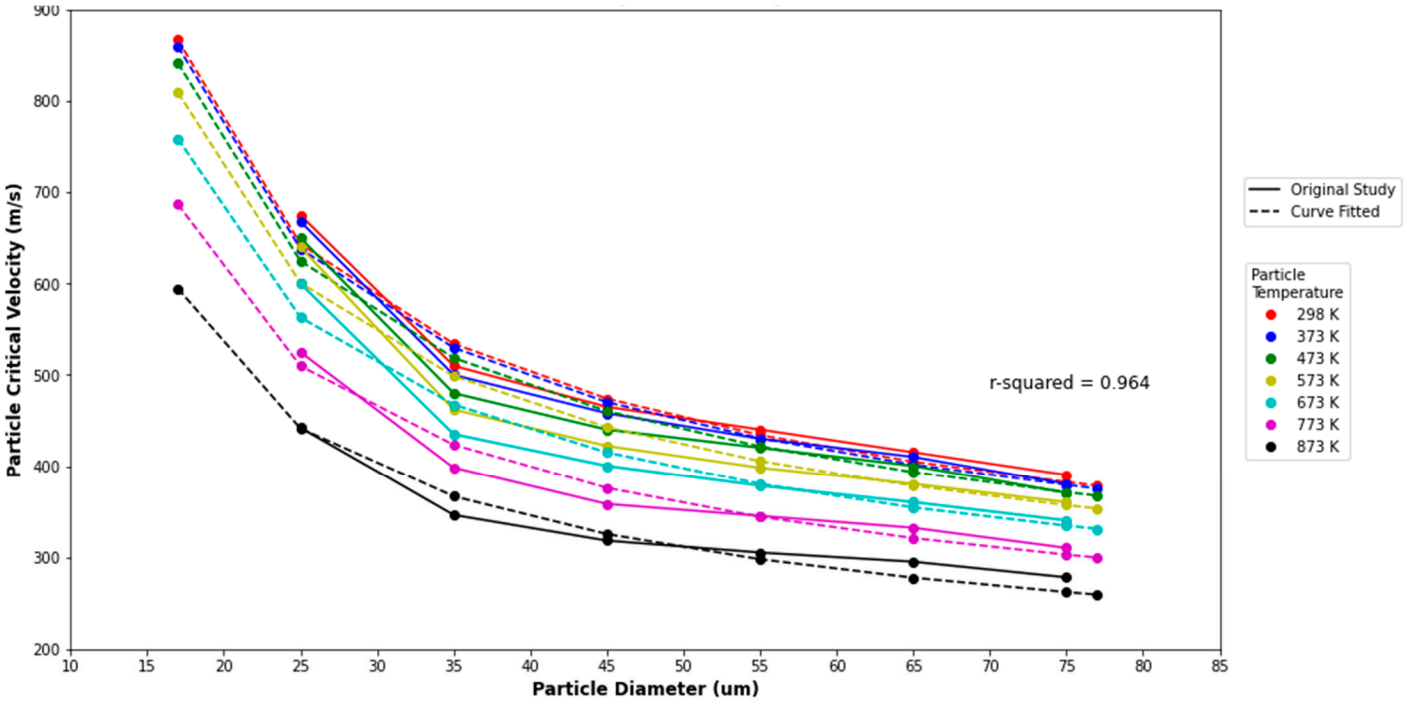


Figure 19. Fitted critical velocity correlation (Equation (1)) vs. original study data [53].

The particle deposition and distribution on the substrate surface are visualized in Figure 20 for the medium-pressure case. The deposited and undeposited particles that landed on the substrate are shown for all four different masks, for each mask SOD and substrate SOD. As can be seen, the particles primarily deposit in the central opening of the mask that is in line with the nozzle centerline. It can also be seen that the masks with smaller rod diameters (Masks 3 and 4) have a wider particle distribution, with a significant number of particles in the adjacent mask openings. However, most of these particles do not deposit. In the high-pressure scenario, nearly all particles are successfully deposited across all test cases (see Figure 21). This emphasizes that the inlet pressure has a dominant impact on the particle velocity and deposition, while other parameters exert secondary effects.

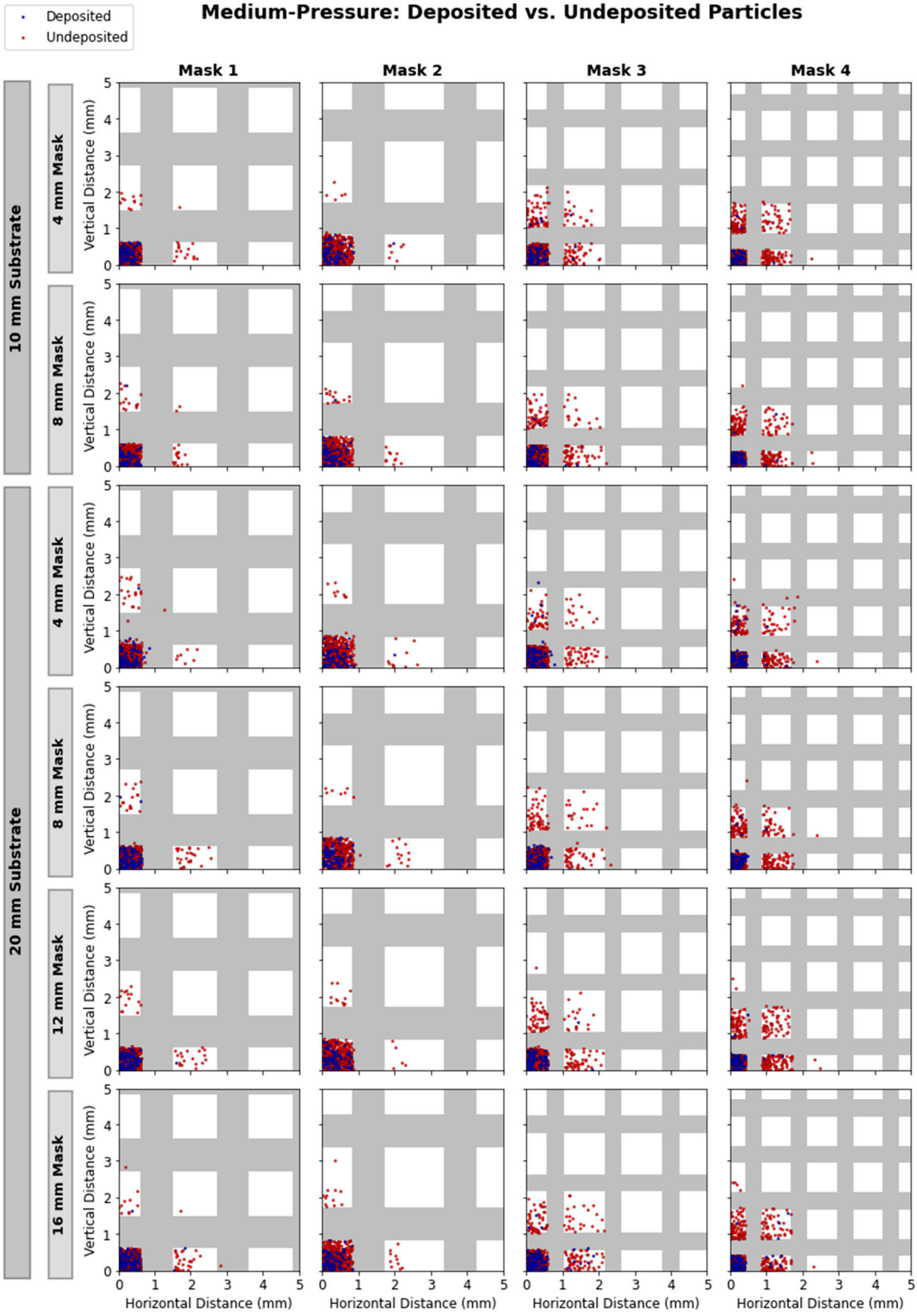


Figure 20. Deposited vs. undeposited particles for each test case (medium pressure case).

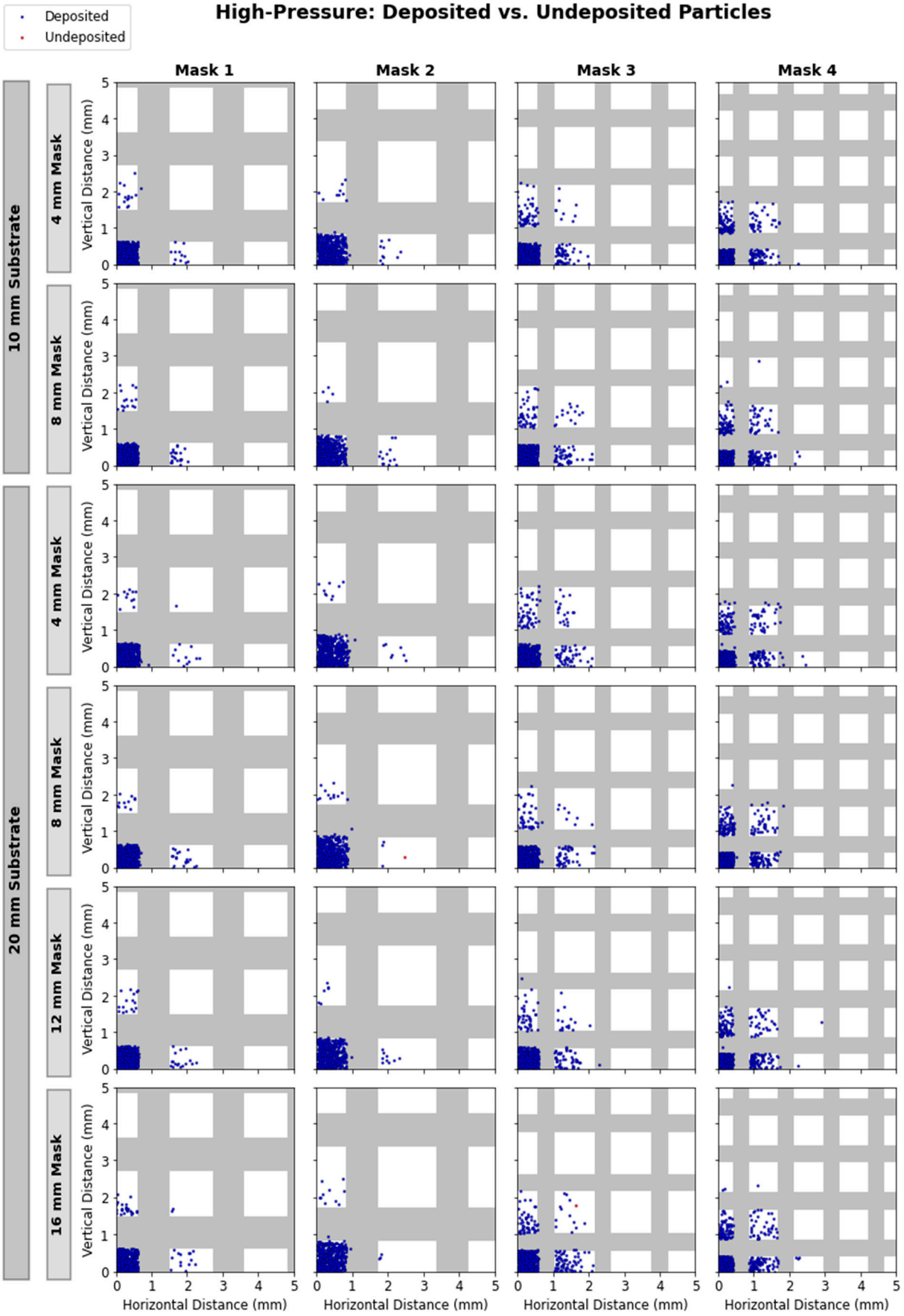


Figure 21. Deposited vs. undeposited particles for each test case (high-pressure case).

The particle deposition efficiency (DE) is shown in Figure 22 for the medium-pressure case. The DE analyzed here is defined as the percentage of particles that deposit on the substrate to the total number of particles that impact the substrate. It is worth noting that the DE for the high-pressure case is greater than 99.9% for all test cases, with almost all the particles depositing. This exceptionally high deposition efficiency aligns with the high-pressure scenario observed in the experimental and numerical study by Garmeh et al. [31], where cold spray was applied to both on-axis and off-axis nozzle/substrate hole geometries. However, for the medium-pressure case, there appears to be a strong linear relationship between the DE and the mask SOD. As the mask distance from the nozzle exit is increased, the DE of the particles appears to linearly increase. This behavior can be seen for all four masks and both 10 mm and 20 mm substrate SODs. This increase in deposition as the mask SOD is increased can be associated with the particle velocity, which increases when the mask is moved further away. The mask properties, such as the wire size and opening area, also affect the DE, with Mask 1 resulting in the highest DE.

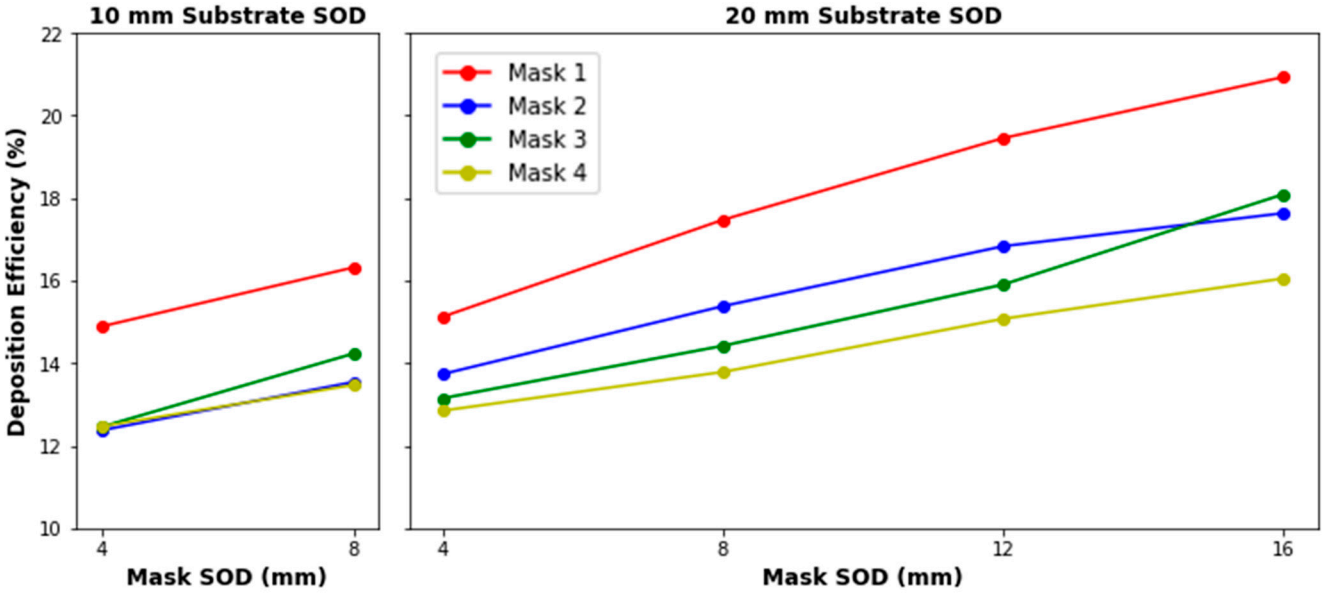


Figure 22. Deposition efficiency for medium-pressure cases.

As discussed, several researchers, including Cormier et al. [23], have experimentally investigated the manufacturability of pyramidal fin arrays using the masked cold spray process. Similar to their work, we considered commercially available masks. However, while their research focused on aluminum and stainless-steel powders for the development of fins in compact heat exchangers [23], our study emphasizes nickel particles due to their relevance in the HER. Consequently, a direct one-to-one comparison is not feasible, but the observed trends can be evaluated. In their work [23], the standoff distances between the substrate, mask, and nozzle were empirically optimized for an inlet pressure of 3 MPa. The cold spray system employed was Plasma Giken PCS-1000, featuring a nozzle with a 3.0 mm throat diameter and a 6.5 mm exit diameter. Through multiple trials, they examined the influence of the standoff distances between the mask and the nozzle, as well as the mask and substrate [23]. While differences existed in nozzle type, powder material, and inlet pressure, both the current study and the work of Cormier et al. [23] demonstrate that maintaining a longer distance between the substrate and the nozzle (approximately 20–25 mm), along with positioning the mask closer to the substrate, is critical for achieving optimal conditions.

4. Conclusions

A numerical parametric analysis was performed on the cold spray process. The deposition and distribution of injected nickel powder were analyzed for the purposes of creating pin fin geometries for a hydrogen electrolysis process. The parametric study analyzed the effects of substrate SOD, mask SOD, mask type, and nozzle inlet operating conditions. Commercially available masks, as used in previous studies, were employed. Although identifying the optimal conditions was challenging due to the interplay of multiple parameters (such as particle type, size, operating conditions, nozzle geometry, and mask configuration), near-optimal deposition conditions for Ni particles were found. Among the analyzed parameters, the nozzle inlet conditions had the most significant impact on particle deposition. Increasing the inlet pressure to 4 MPa achieved a deposition efficiency (DE) of 99%, consistent with our previous findings [31]. This high-pressure inlet condition enhanced the gas flow velocity, both inside and outside the nozzle, resulting in a higher particle impact velocity. At this high pressure, the mask type and standoff distance did not affect the DE, making 4 MPa the optimal condition. If achieving 4 MPa is not feasible, optimal deposition at lower pressures, such as 2 MPa, requires a longer nozzle-to-substrate SOD (approximately 20 mm) and the mask positioned closer to the substrate. These findings align with the experimental results of Cormier et al. [23], who experimentally demonstrated an improved deposition for aluminum and stainless-steel particles under reduced pressures. However, at a medium pressure (2 MPa), the DE ranged from 12 to 21%. It was also found that the DE increased linearly as the mask SOD increased. This relationship is due to the higher average particle velocity that was achieved when the mask SOD was increased. It was found that the average velocity of the particles before entering the mask slightly increased, also linearly, when the mask SOD was increased. This was due to the particles being allowed to accelerate for a longer period. Regarding the particle distribution and deposition, it was shown that the nickel particles deposited primarily in the central opening of the mask (i.e., mask opening in line with nozzle centerline). While this study focused on key process parameters, future work should investigate the influence of particle feedstock nonuniformity, including sphericity, to further refine the understanding of particle dynamics and deposition outcomes.

Author Contributions: Conceptualization, A.D. and M.J.; methodology, N.N. and M.J.; software, N.N.; writing—original draft preparation, N.N.; writing—review and editing, A.D. and M.J. All authors have read and agreed to the published version of the manuscript.

Funding: This research received no external funding.

Institutional Review Board Statement: Not applicable.

Informed Consent Statement: Not applicable.

Data Availability Statement: The raw data supporting the conclusions of this article will be made available by the authors on request.

Conflicts of Interest: The authors declare no conflicts of interest.

Appendix A. The Mesh Sensitivity Analysis

To ensure that the solution was independent of the mesh, two different mesh dependency studies were performed. The first mesh study was conducted to analyze the overall flow behavior in the nozzle and external domain to ensure that flow features such as shocks were accurately captured. The three following different mesh resolutions were analyzed: coarse (730,000 cells), fine (1,420,000 cells), and very fine (2,980,000 cells). The mesh at the nozzle, mask, and substrate walls was kept consistent for all three resolutions. The gas pressure and velocity profiles were compared along the centerline of the geometry, as shown in Figures A1 and A2, respectively. As can be seen, all three mesh resolutions were able to adequately model the flow in the nozzle, as well as capture the shocks at the nozzle exit, as indicated by the sharp increase in pressure and decrease in velocity downstream of

the nozzle exit. Therefore, to save computational costs, the flow could be modelled with the coarse mesh resolution.

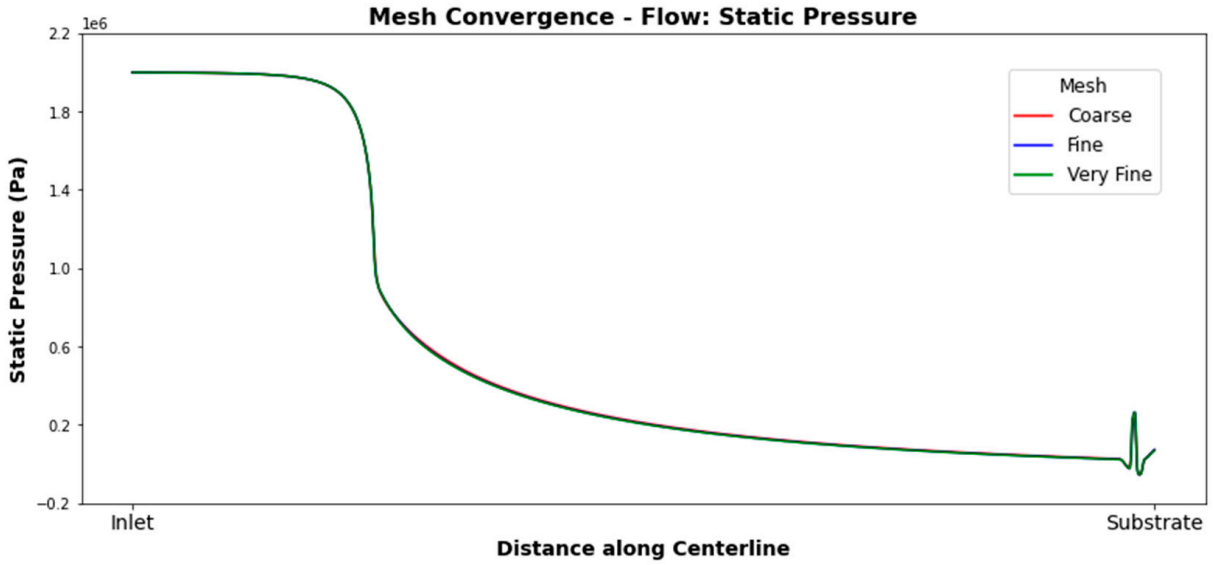


Figure A1. Mesh convergence of flow—gas static pressure along the centerline.

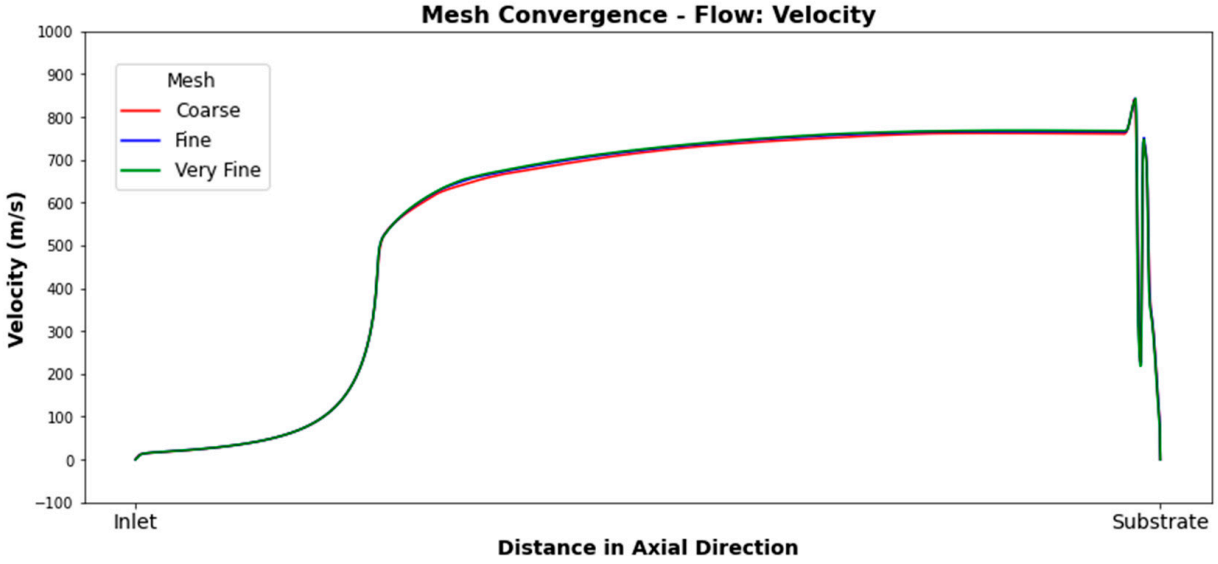


Figure A2. Mesh convergence of flow—gas velocity along the centerline.

A secondary mesh refinement study was performed, which focused on the near-wall region, specifically near the mask walls and near the substrate surface. As discussed, the SST k-ω turbulence model was used for the analysis, which performs well with a fully resolved near-wall mesh. Therefore, to ensure that the near-wall mesh was sufficiently resolved, three different meshes with varying average y+ values were analyzed. The y+ is a non-dimensional value that corresponds to the height of the first cell center adjacent to the wall. The mesh characteristics for the three different cases are shown in Table A1. To analyze the flow, the gas pressure and velocity profiles were examined along a line through the mask rods, from the nozzle exit to the substrate. The respective profiles are shown below in Figures A3 and A4. As can be seen, the profiles are similar for all three meshes. However, as will be discussed in Appendix B, the fine and very fine meshes are better able to resolve the flow near and downstream of the mask. Therefore, the near-wall mesh at the mask is refined inline with the very fine resolution, with an average y+ of less than 1.

Table A1. Mesh characteristics.

Wall Mesh	# of Cells	Average Mask Wall y+
Coarse	1,030,000	12.10
Fine	1,280,000	6.86
Very Fine	1,900,000	0.53

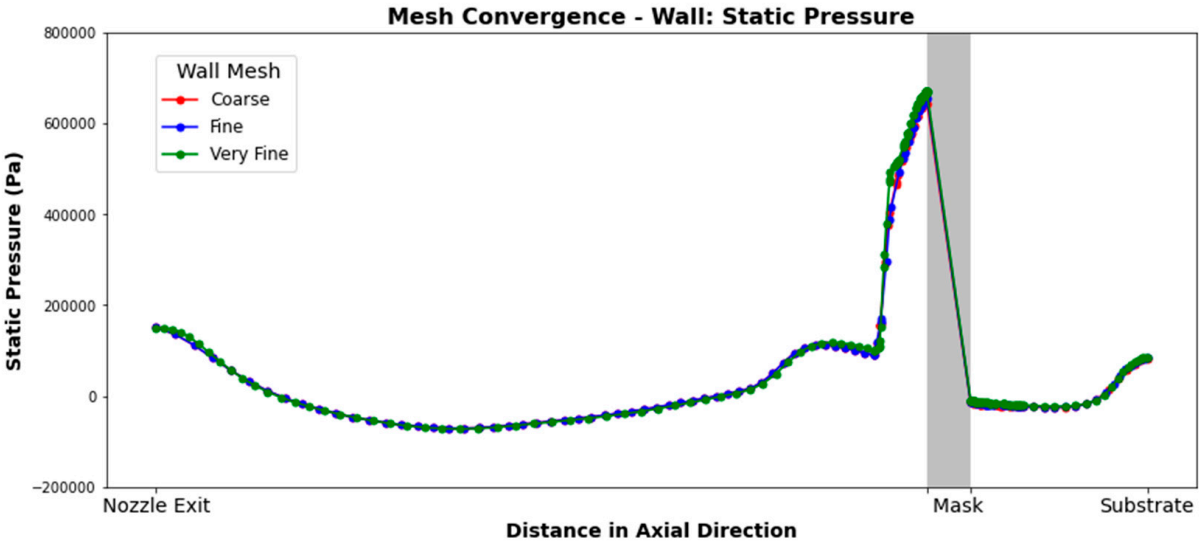


Figure A3. Convergence of near wall mesh—gas static pressure in the axial direction.

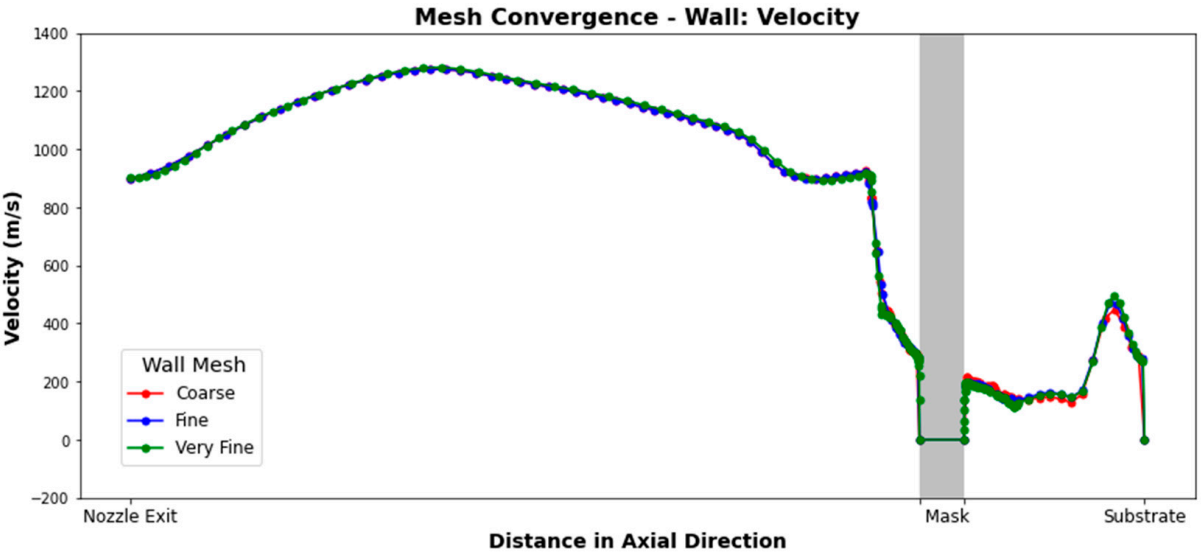


Figure A4. Convergence of near wall mesh—gas velocity in the axial direction.

Appendix B. A Comparison of the k-ε Realizable and SST k-ω Models

The SST k-ω model is typically better at analyzing the near-wall flow behavior of the supersonic flow around cylinders (i.e., the mask rods) as compared to k-ε models with default wall functions. Benim et al. [54] analyzed the supersonic flow around cylinders and found that the drag coefficient was poorly modeled by the k-ε models with a wall function. On the other hand, the SST k-ω model with a fully resolved wall mesh was significantly better at modeling the near-wall behavior by more accurately capturing the drag coefficient and boundary-layer effects. However, the SST k-ω model requires a sufficiently refined near-wall mesh. As a general rule, a dimensionless y+ value of less than 1 is recommended

to adequately solve the near-wall flow [54]. A y+ value of 1 would ensure that the first cell is located within the viscous sublayer, allowing for the flow in the boundary layer to be resolved. Since the interest of this study is in the flow behavior around the mask and at the substrate surface, the mesh was sufficiently refined such that the average y+ value was less than 1 for those regions. It should also be noted that the SST k-ω model implements wall formulations (i.e., y+ insensitive near-wall treatment) to minimize variations where the y+ is outside the viscous sublayer [45].

A comparison of the k-ε realizable and SST k-ω model was performed, as shown in Figure A5. The figure shows the gas pressure, velocity, and temperature contours for both the k-ε realizable and SST k-ω turbulence models. For the comparison, the high-pressure case with a 20 mm substrate SOD and 16 mm mask SOD was used. As can be seen, the flow upstream of the mask is almost identical for both models, however, the flow near and downstream of the mask is significantly different. The SST k-ω model appears to more accurately capture the expected wake behind the mask cylinders. The SST k-ω model also appears to better capture the pressure build-up at the substrate surface in the stagnation zone. This comparison is consistent with the results of Benim et al. [54] and shows that the use of k-ε model with wall functions is not adequate to capture the fluid mixing and flow separation that occurs downstream of the mask.

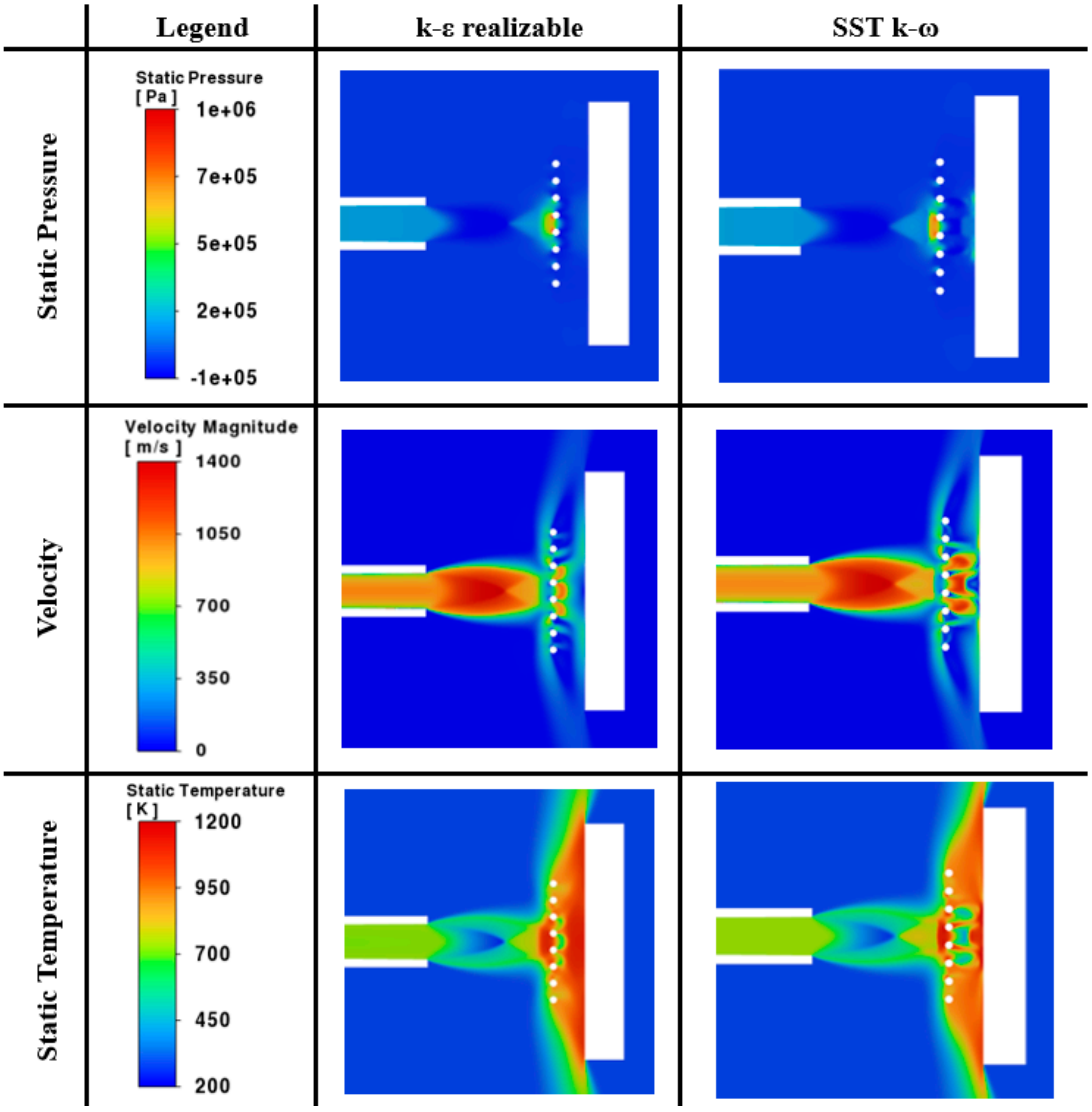


Figure A5. Turbulence model comparison.

Appendix C. Flow Contours for Masks 1 and 3 (Medium and High Pressures)

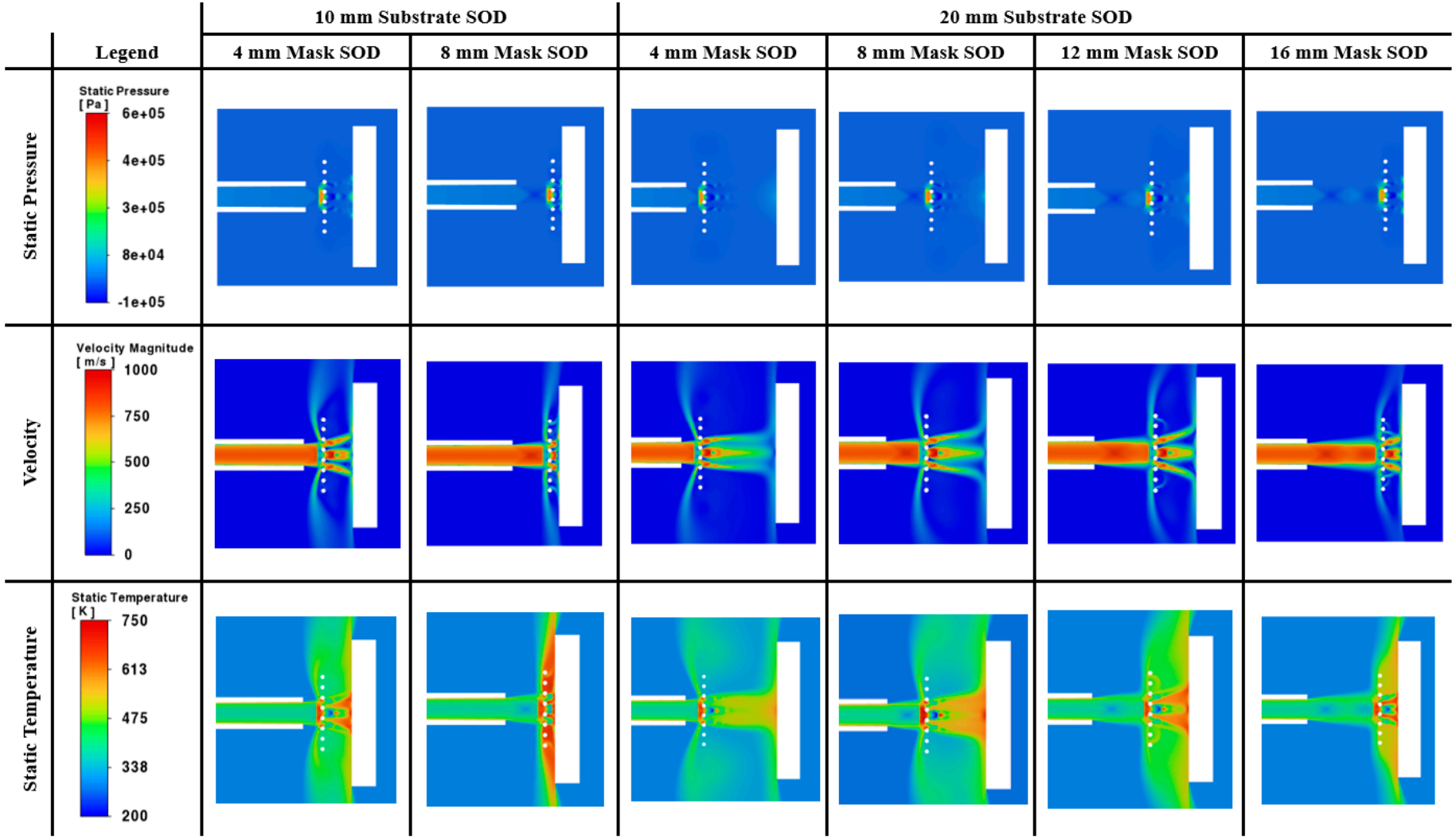


Figure A6. Flow contours for Mask 1 (medium-pressure case).

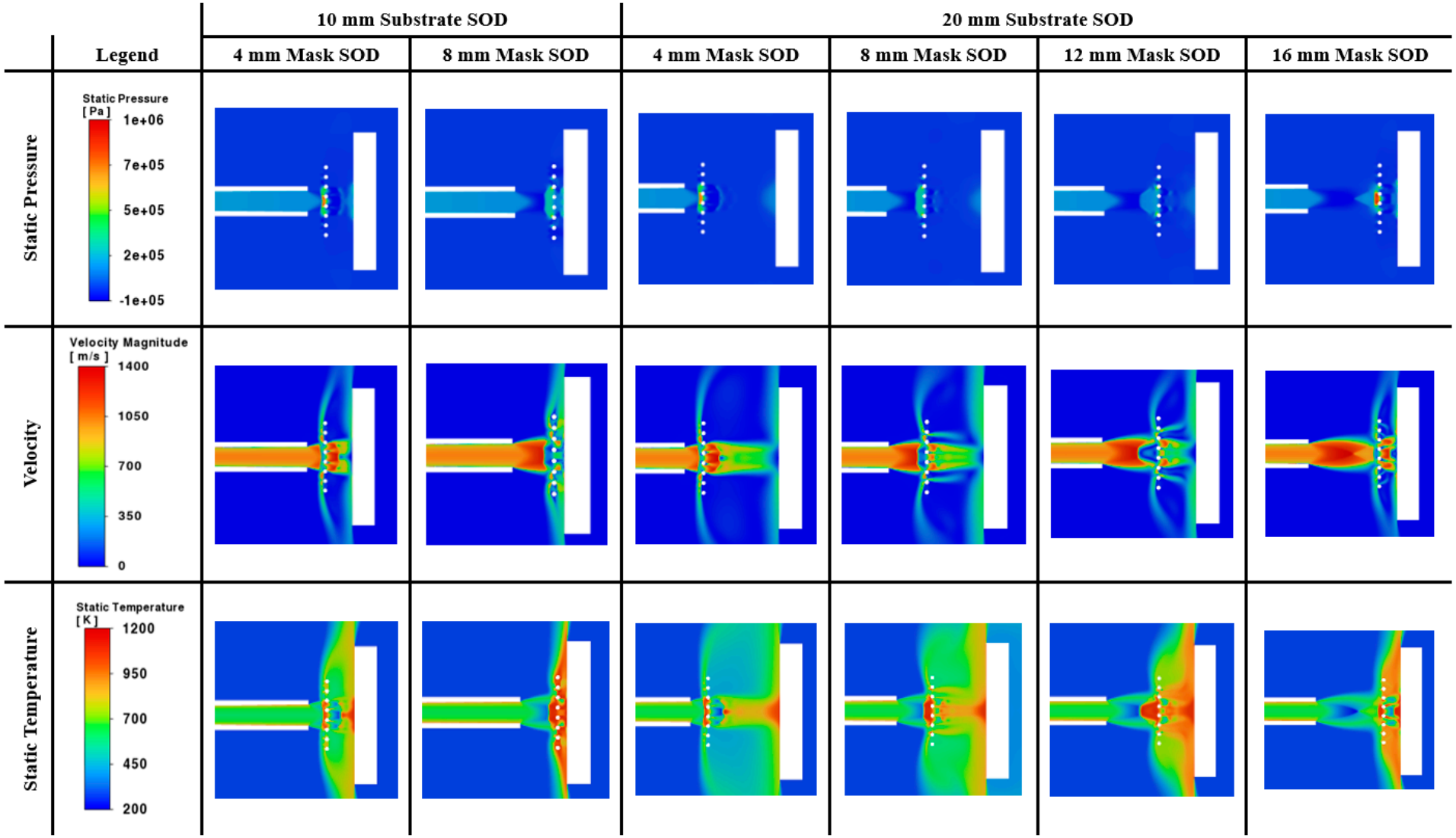


Figure A7. Flow contours for Mask 1 (high-pressure case).

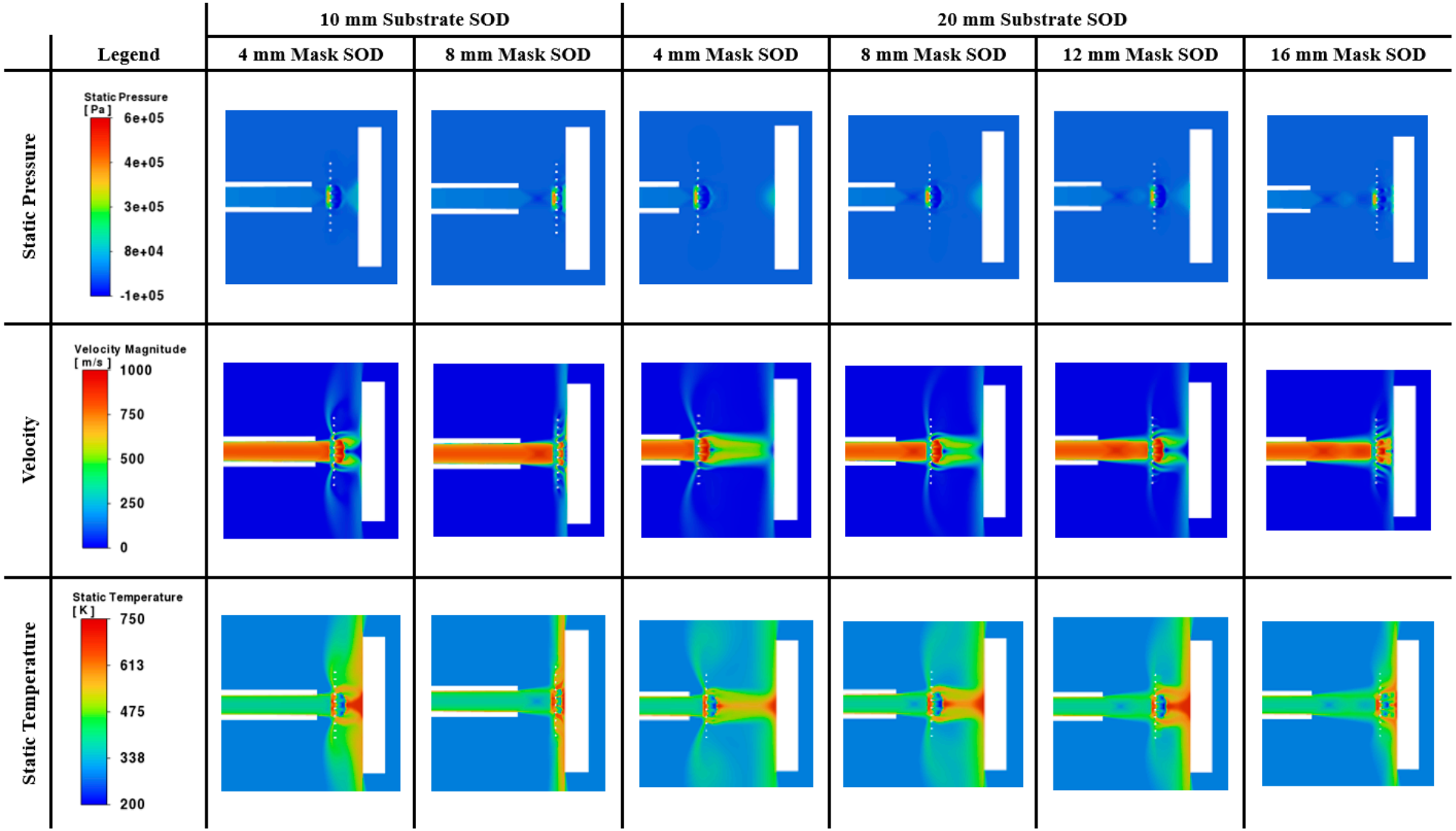


Figure A8. Flow contours for Mask 3 (medium-pressure case).

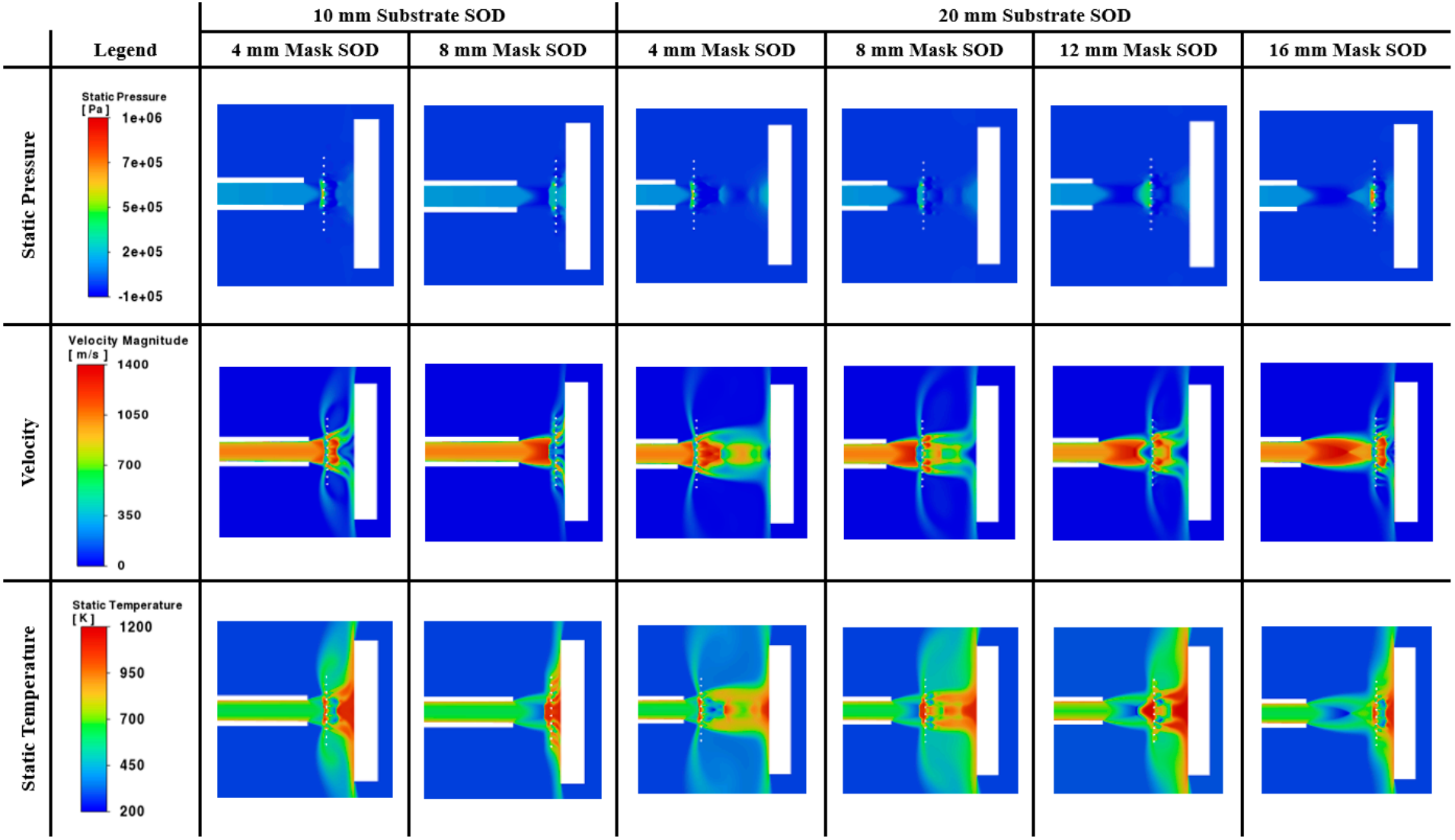


Figure A9. Flow contours for Mask 3 (high-pressure case).

Appendix D. Gas Velocity and Pressure Profiles Along the Jet Centerline (High-Pressure Case)

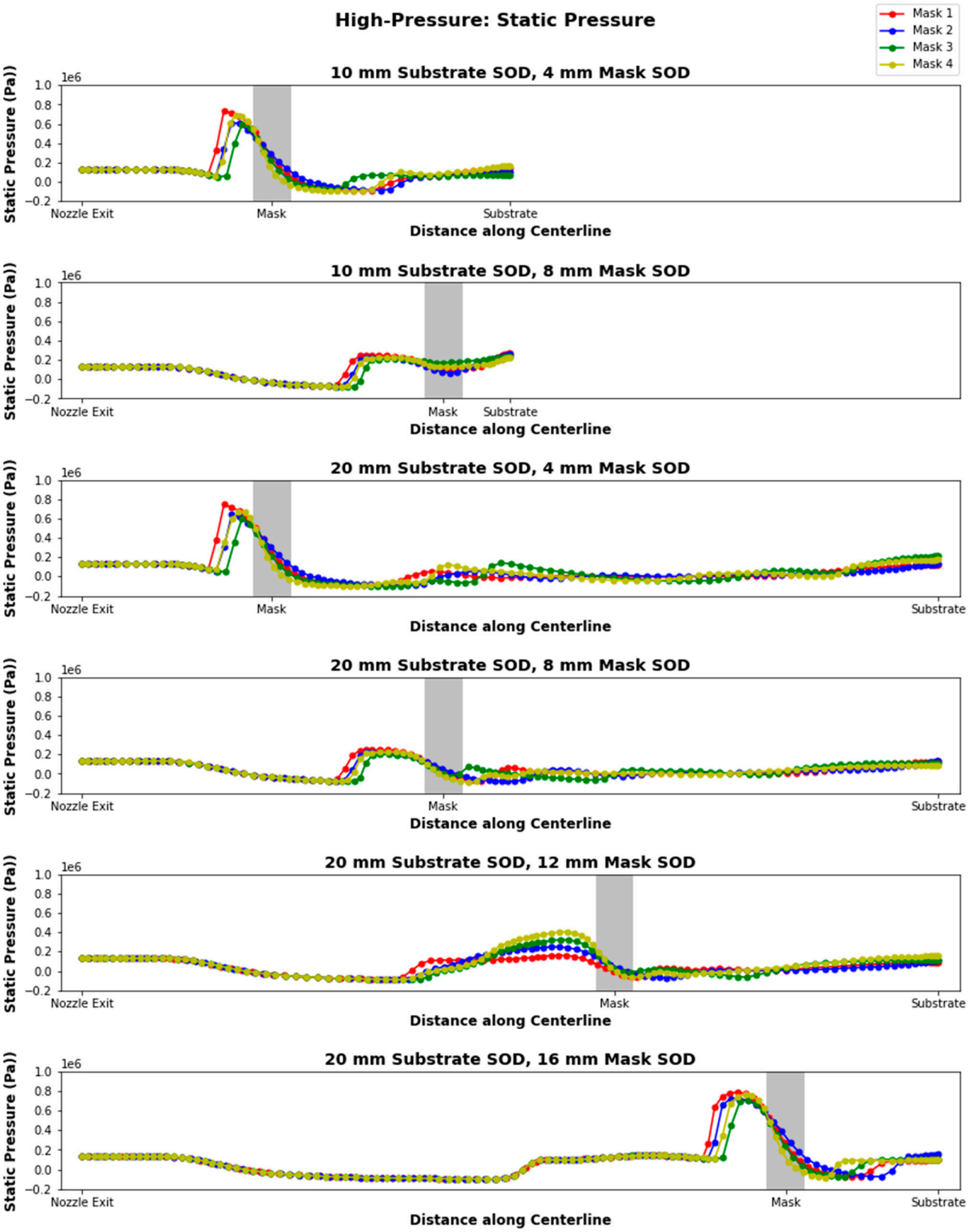


Figure A10. Gas pressure profile along centerline (high-pressure case).

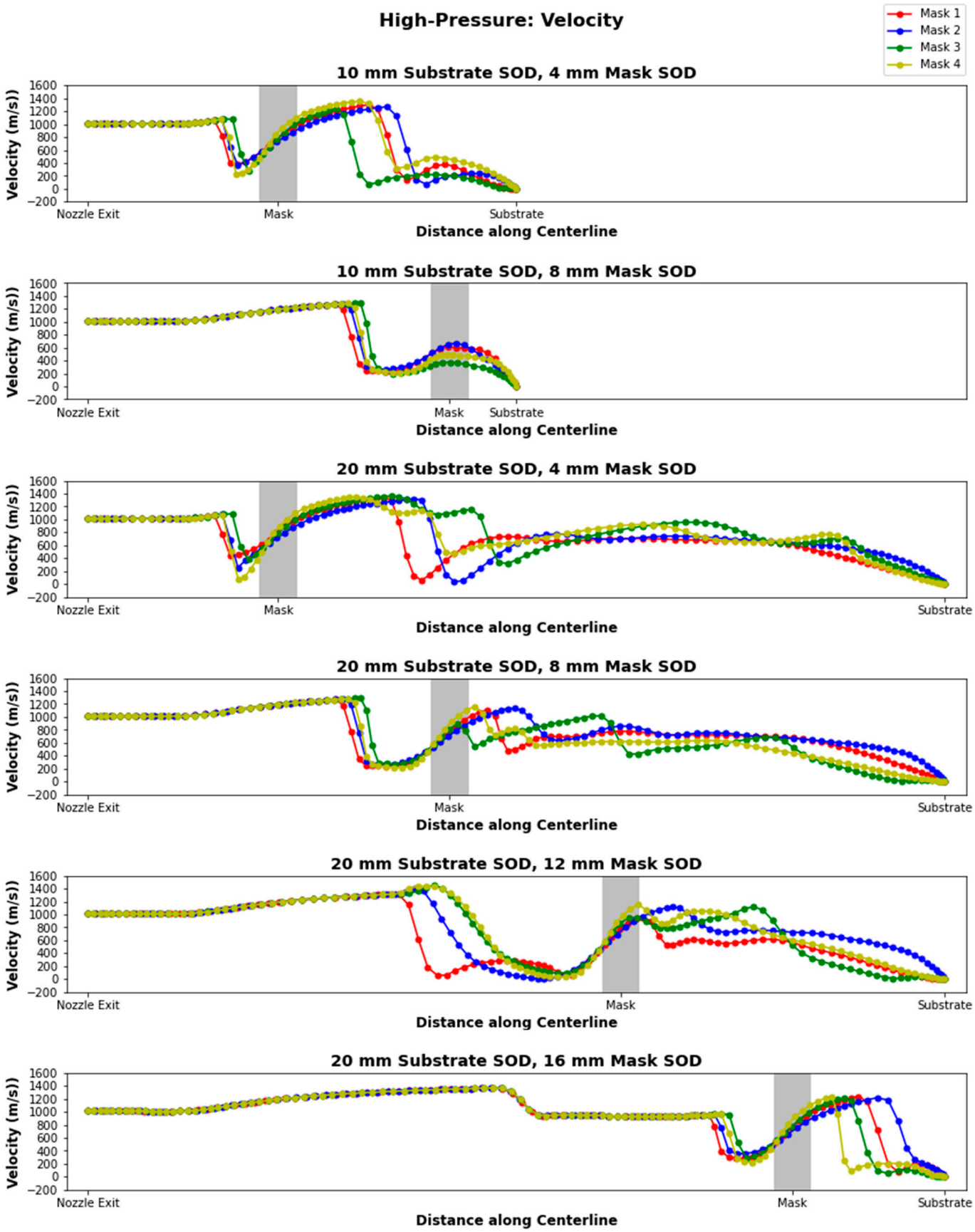


Figure A11. Gas velocity profile along centerline (high-pressure case).

Appendix E. Gas Temperature Profiles Along the Jet Centerline

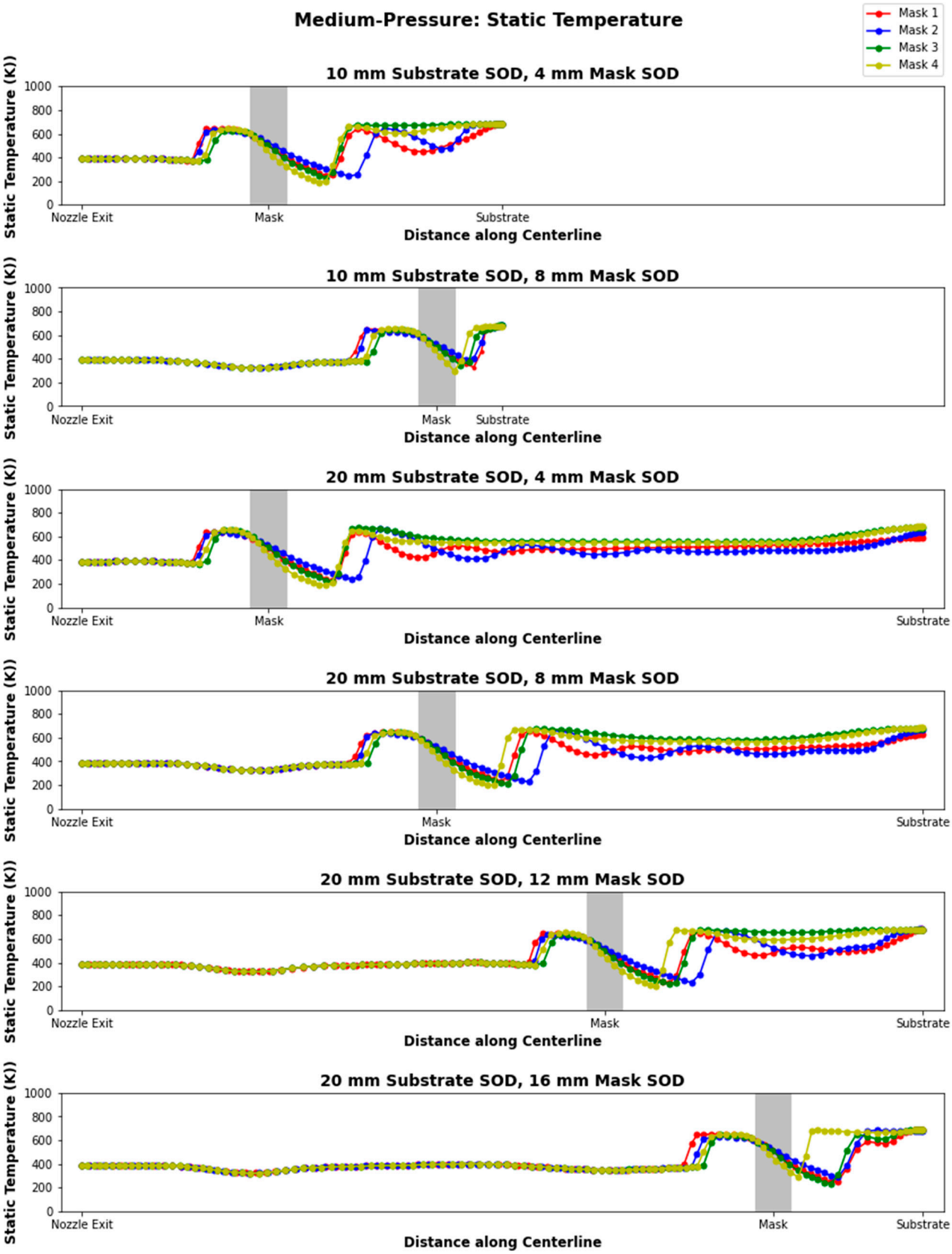


Figure A12. Gas temperature profile along centerline (medium-pressure case).

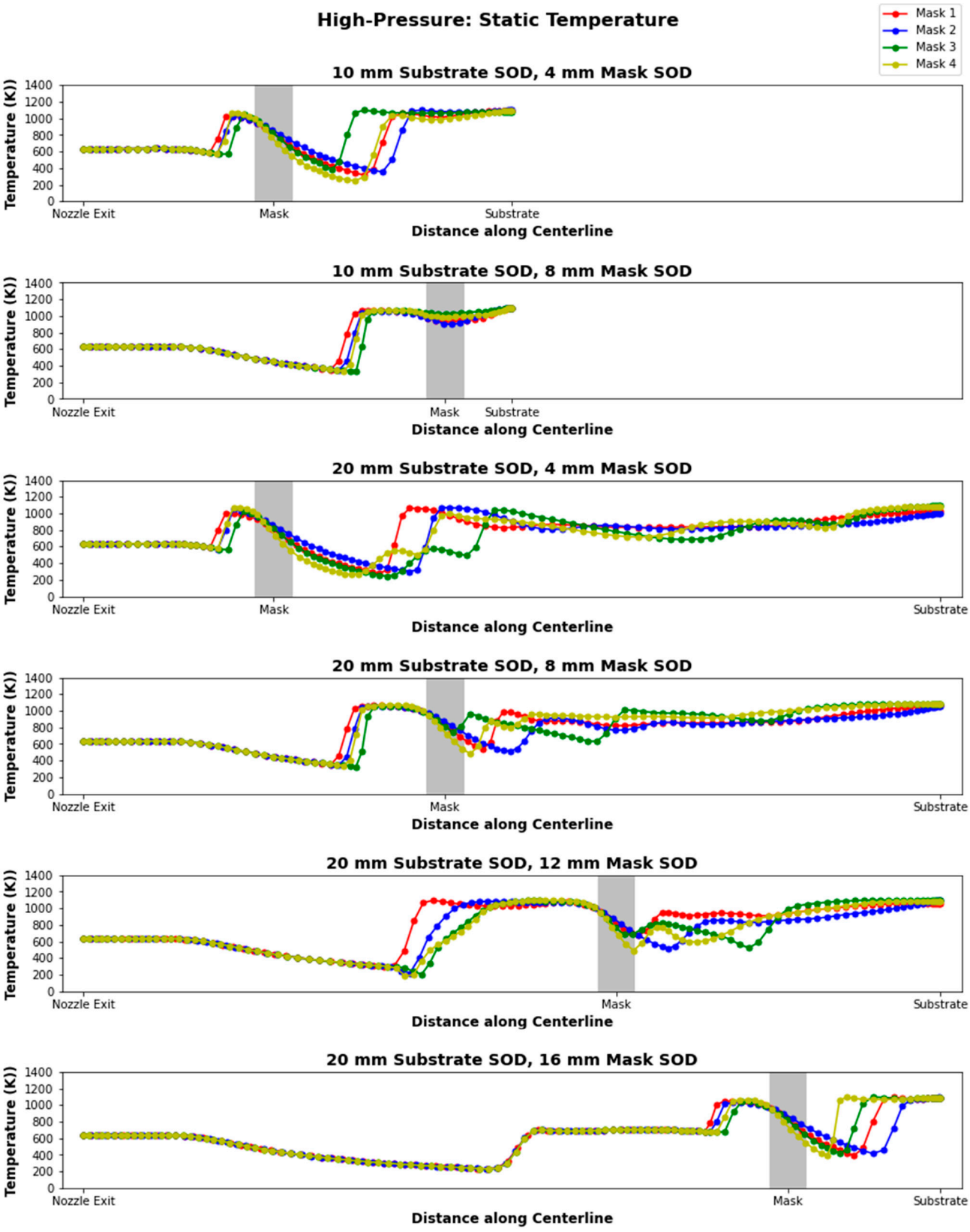


Figure A13. Gas temperature profile along centerline (high-pressure case).

Appendix F. The Average Particle Temperature for Medium-Pressure and High-Pressure Cases

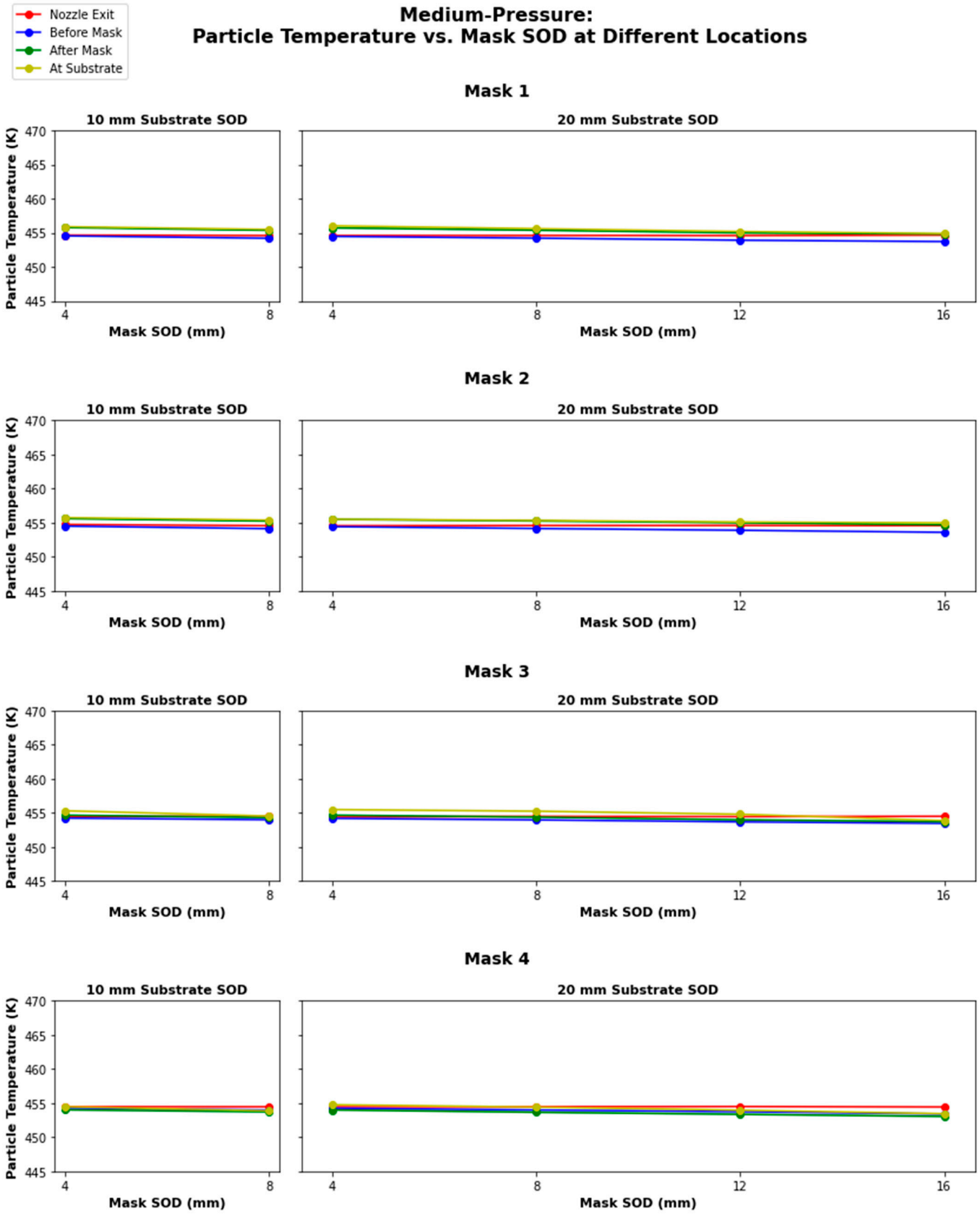


Figure A14. Average particle temperature at different locations (medium-pressure case).

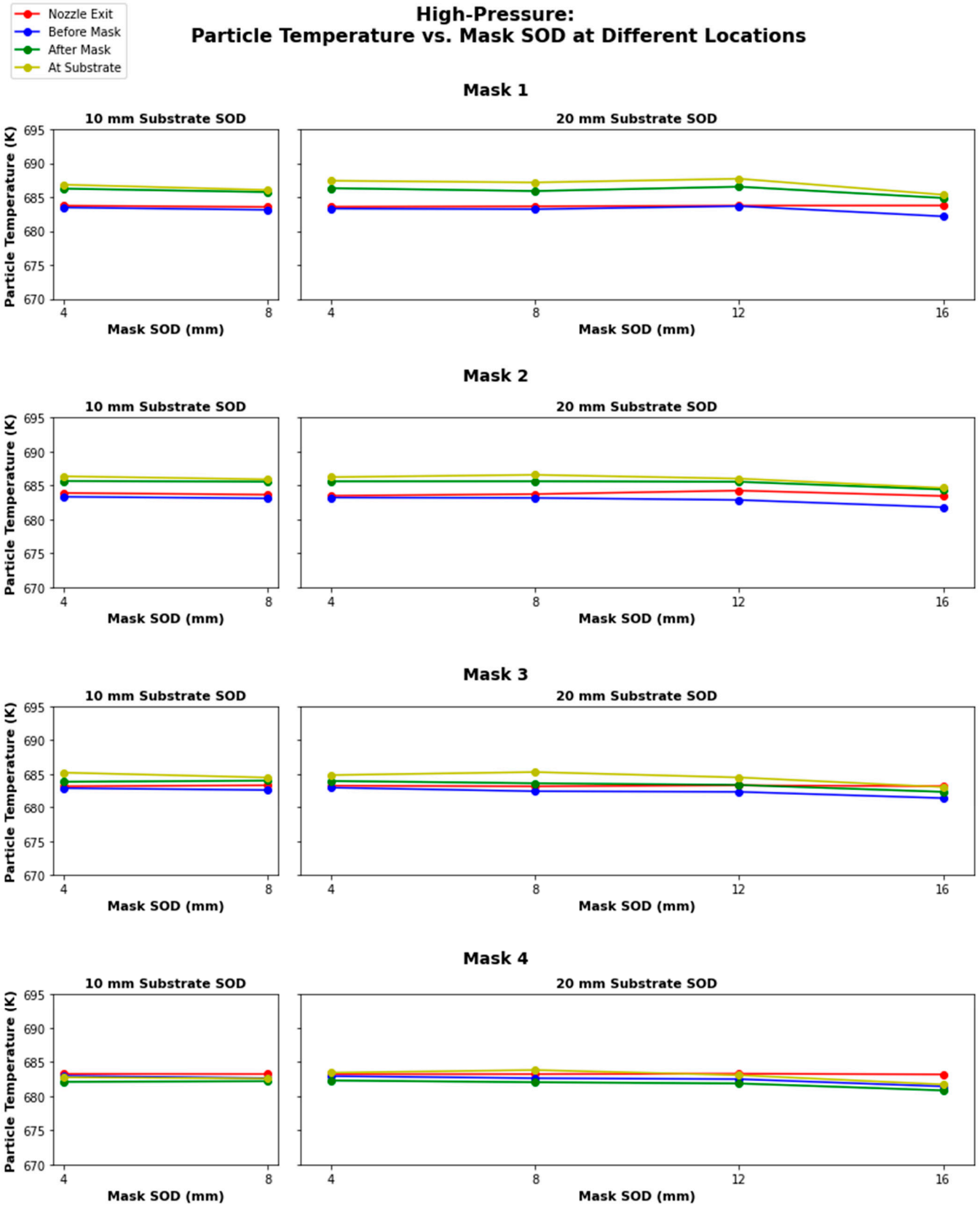


Figure A15. Average particle temperature at different locations (high-pressure case).

Appendix G. Particle Distribution at Various Locations (Mask 1, 16 mm Mask SOD, 20 mm Substrate SOD) for the High-Pressure Case

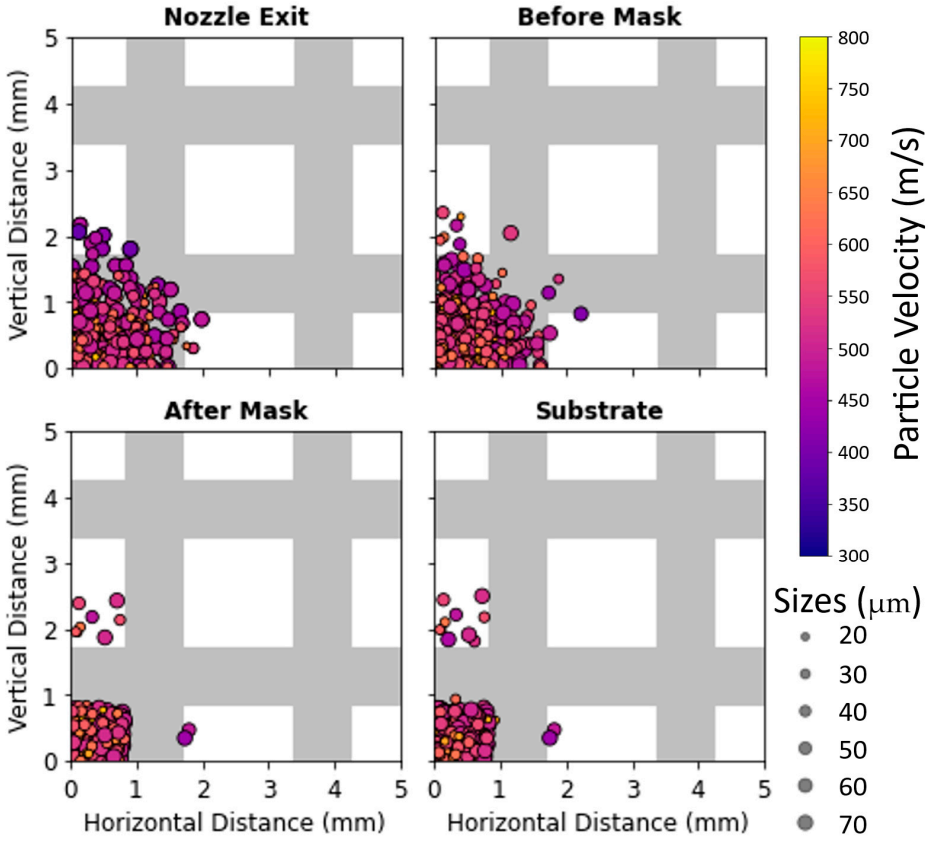


Figure A16. Particle distribution at different locations: Mask 1, 16 mm Mask SOD, 20 mm substrate SOD, high-pressure case.

References

1. Ashokkumar, M.; Thirumalaikumarasamy, D.; Sonar, T.; Deepak, S.; Vignesh, P.; Anbarasu, M. An Overview of Cold Spray Coating in Additive Manufacturing, Component Repairing and Other Engineering Applications. *J. Mech. Behav. Mater.* **2022**, *31*, 514–534. [CrossRef]
2. Fauchais, P.L.; Heberlein, J.V.R.; Boulos, M.I. *Thermal Spray Fundamentals*; Springer US: Boston, MA, USA, 2014; ISBN 978-0-387-28319-7.
3. Vardelle, A.; Moreau, C.; Akedo, J.; Ashrafizadeh, H.; Berndt, C.C.; Berghaus, J.O.; Boulos, M.; Brogan, J.; Bourtsalas, A.C.; Dolatabadi, A.; et al. The 2016 Thermal Spray Roadmap. *J. Therm. Spray Technol.* **2016**, *25*, 1376–1440. [CrossRef]
4. Cavaliere, P. *Cold-Spray Coatings*; Cavaliere, P., Ed.; Springer International Publishing: Cham, Switzerland, 2018; ISBN 978-3-319-67182-6.
5. Grujicic, M.; Zhao, C.L.; DeRosset, W.S.; Helfritch, D. Adiabatic Shear Instability Based Mechanism for Particles/Substrate Bonding in the Cold-Gas Dynamic-Spray Process. *Mater. Des.* **2004**, *25*, 681–688. [CrossRef]
6. Klinkov, S.V.; Kosarev, V.F.; Rein, M. Cold Spray Deposition: Significance of Particle Impact Phenomena. *Aerosp. Sci. Technol.* **2005**, *9*, 582–591. [CrossRef]
7. Sova, A.; Okunkova, A.; Grigoriev, S.; Smurov, I. Velocity of the Particles Accelerated by a Cold Spray Micronozzle: Experimental Measurements and Numerical Simulation. *J. Therm. Spray Technol.* **2013**, *22*, 75–80. [CrossRef]
8. Yin, S.; Sun, Y.; Wang, X.; Guo, Z.; Liao, H. Effect of Spray Angle on Temperature Distribution within the Metallic Substrate in Cold Spraying. *J. Therm. Spray Technol.* **2013**, *22*, 983–991. [CrossRef]
9. Yin, S.; Liu, Q.; Liao, H.; Wang, X. Effect of Injection Pressure on Particle Acceleration, Dispersion and Deposition in Cold Spray. *Comput. Mater. Sci.* **2014**, *90*, 7–15. [CrossRef]
10. Yin, S.; Suo, X.; Liao, H.; Guo, Z.; Wang, X. Significant Influence of Carrier Gas Temperature during the Cold Spray Process. *Surf. Eng.* **2014**, *30*, 443–450. [CrossRef]
11. Assadi, H.; Gärtner, F.; Stoltenhoff, T.; Kreye, H. Bonding Mechanism in Cold Gas Spraying. *Acta Mater.* **2003**, *51*, 4379–4394. [CrossRef]

12. Schmidt, T.; Assadi, H.; Gärtner, F.; Richter, H.; Stoltenhoff, T.; Kreye, H.; Klassen, T. From Particle Acceleration to Impact and Bonding in Cold Spraying. *J. Therm. Spray Technol.* **2009**, *18*, 794. [CrossRef]
13. Vaz, R.; Garfias, A.; Albaladejo, V.; Sanchez, J.; Cano, I. A Review of Advances in Cold Spray Additive Manufacturing. *Coatings* **2023**, *13*, 267. [CrossRef]
14. Meng, Y.; Saito, H.; Bernard, C.; Ichikawa, Y.; Ogawa, K. Optimal Design of a Cold Spray Nozzle for Inner Wall Coating Fabrication by Combining CFD Simulation and Neural Networks. *J. Therm. Spray Technol.* **2024**, *33*, 3–16. [CrossRef]
15. Faizan-Ur-Rab, M.; Zahiri, S.H.; King, P.C.; Busch, C.; Masood, S.H.; Jahedi, M.; Nagarajah, R.; Gulizia, S. Utilization of Titanium Particle Impact Location to Validate a 3D Multicomponent Model for Cold Spray Additive Manufacturing. *J. Therm. Spray Technol.* **2017**, *26*, 1874–1887. [CrossRef]
16. Aghasibeig, M.; Monajatizadeh, H.; Bocher, P.; Dolatabadi, A.; Wuthrich, R.; Moreau, C. Cold Spray as a Novel Method for Development of Nickel Electrode Coatings for Hydrogen Production. *Int. J. Hydrogen Energy* **2016**, *41*, 227–238. [CrossRef]
17. Wang, S.; Lu, A.; Zhong, C.-J. Hydrogen Production from Water Electrolysis: Role of Catalysts. *Nano Converg.* **2021**, *8*, 4. [CrossRef]
18. Aghasibeig, M.; Moreau, C.; Dolatabadi, A.; Wuthrich, R. Engineered Three-Dimensional Electrodes by HVOF Process for Hydrogen Production. *J. Therm. Spray Technol.* **2016**, *25*, 1561–1569. [CrossRef]
19. Aghasibeig, M.; Dolatabadi, A.; Wuthrich, R.; Moreau, C. Three-Dimensional Electrode Coatings for Hydrogen Production Manufactured by Combined Atmospheric and Suspension Plasma Spray. *Surf. Coat. Technol.* **2016**, *291*, 348–355. [CrossRef]
20. Dupuis, P.; Cormier, Y.; Farjam, A.; Jodoin, B.; Corbeil, A. Performance Evaluation of Near-Net Pyramidal Shaped Fin Arrays Manufactured by Cold Spray. *Int. J. Heat Mass Transf.* **2014**, *69*, 34–43. [CrossRef]
21. Cormier, Y.; Dupuis, P.; Jodoin, B.; Corbeil, A. Pyramidal Fin Arrays Performance Using Streamwise Anisotropic Materials by Cold Spray Additive Manufacturing. *J. Therm. Spray Technol.* **2016**, *25*, 170–182. [CrossRef]
22. Dupuis, P.; Cormier, Y.; Fenech, M.; Corbeil, A.; Jodoin, B. Flow Structure Identification and Analysis in Fin Arrays Produced by Cold Spray Additive Manufacturing. *Int. J. Heat Mass Transf.* **2016**, *93*, 301–313. [CrossRef]
23. Cormier, Y.; Dupuis, P.; Jodoin, B.; Corbeil, A. Net Shape Fins for Compact Heat Exchanger Produced by Cold Spray. *J. Therm. Spray Technol.* **2013**, *22*, 1210–1221. [CrossRef]
24. Dupuis, P.; Cormier, Y.; Fenech, M.; Jodoin, B. Heat Transfer and Flow Structure Characterization for Pin Fins Produced by Cold Spray Additive Manufacturing. *Int. J. Heat Mass Transf.* **2016**, *98*, 650–661. [CrossRef]
25. Cormier, Y.; Dupuis, P.; Farjam, A.; Corbeil, A.; Jodoin, B. Additive Manufacturing of Pyramidal Pin Fins: Height and Fin Density Effects under Forced Convection. *Int. J. Heat Mass Transf.* **2014**, *75*, 235–244. [CrossRef]
26. Farjam, A.; Cormier, Y.; Dupuis, P.; Jodoin, B.; Corbeil, A. Influence of Alumina Addition to Aluminum Fins for Compact Heat Exchangers Produced by Cold Spray Additive Manufacturing. *J. Therm. Spray Technol.* **2015**, *24*, 1256–1268. [CrossRef]
27. Meyer, M.; Lupoi, R. An Analysis of the Particulate Flow in Cold Spray Nozzles. *Mech. Sci.* **2015**, *6*, 127–136. [CrossRef]
28. Meyer, M.C.; Yin, S.; McDonnell, K.A.; Stier, O.; Lupoi, R. Feed Rate Effect on Particulate Acceleration in Cold Spray under Low Stagnation Pressure Conditions. *Surf. Coat. Technol.* **2016**, *304*, 237–245. [CrossRef]
29. Song, J.; Liu, J.; Chen, Q.; Li, K. Effect of the Shape Factor on the Cold-Spraying Dynamic Characteristics of Sprayed Particles. *J. Therm. Spray Technol.* **2017**, *26*, 1851–1858. [CrossRef]
30. Pattison, J.; Celotto, S.; Khan, A.; O'Neill, W. Standoff Distance and Bow Shock Phenomena in the Cold Spray Process. *Surf. Coat. Technol.* **2008**, *202*, 1443–1454. [CrossRef]
31. Garmeh, S.; Jadidi, M.; Lamarre, J.-M.; Dolatabadi, A. Cold Spray Gas Flow Dynamics for On and Off-Axis Nozzle/Substrate Hole Geometries. *J. Therm. Spray Technol.* **2023**, *32*, 208–225. [CrossRef]
32. Garmeh, S.; Jadidi, M. Numerical Study on Particle Behavior and Deposition Accuracy in Cold Spray Additive Manufacturing. *Coatings* **2022**, *12*, 1546. [CrossRef]
33. Garmeh, S.; Jadidi, M.; Dolatabadi, A. Three-Dimensional Modeling of Cold Spray for Additive Manufacturing. *J. Therm. Spray Technol.* **2020**, *29*, 38–50. [CrossRef]
34. Li, S.; Muddle, B.; Jahedi, M.; Soria, J. A Numerical Investigation of the Cold Spray Process Using Underexpanded and Overexpanded Jets. *J. Therm. Spray Technol.* **2012**, *21*, 108–120. [CrossRef]
35. Liebersbach, P.; Foelsche, A.; Champagne, V.K.; Siopis, M.; Nardi, A.; Schmidt, D.P. CFD Simulations of Feeder Tube Pressure Oscillations and Prediction of Clogging in Cold Spray Nozzles. *J. Therm. Spray Technol.* **2020**, *29*, 400–412. [CrossRef]
36. Gabor, T.; Akin, S.; Jun, M.B.G. Numerical Studies on Cold Spray Gas Dynamics and Powder Flow in Circular and Rectangular Nozzles. *J. Manuf. Process.* **2024**, *114*, 232–246. [CrossRef]
37. Suo, X.K.; Liu, T.K.; Li, W.Y.; Suo, Q.L.; Planche, M.P.; Liao, H.L. Numerical Study on the Effect of Nozzle Dimension on Particle Distribution in Cold Spraying. *Surf. Coat. Technol.* **2013**, *220*, 107–111. [CrossRef]
38. Yin, S.; Zhang, M.; Guo, Z.; Liao, H.; Wang, X. Numerical Investigations on the Effect of Total Pressure and Nozzle Divergent Length on the Flow Character and Particle Impact Velocity in Cold Spraying. *Surf. Coat. Technol.* **2013**, *232*, 290–297. [CrossRef]
39. Sova, A.; Grigoriev, S.; Kochetkova, A.; Smurov, I. Influence of Powder Injection Point Position on Efficiency of Powder Preheating in Cold Spray: Numerical Study. *Surf. Coat. Technol.* **2014**, *242*, 226–231. [CrossRef]
40. Huang, G.; Gu, D.; Li, X.; Xing, L.; Wang, H. Numerical Simulation on Syphonage Effect of Laval Nozzle for Low Pressure Cold Spray System. *J. Mater. Process. Technol.* **2014**, *214*, 2497–2504. [CrossRef]
41. Ozdemir, O.C.; Widener, C.A.; Carter, M.J.; Johnson, K.W. Predicting the Effects of Powder Feeding Rates on Particle Impact Conditions and Cold Spray Deposited Coatings. *J. Therm. Spray Technol.* **2017**, *26*, 1598–1615. [CrossRef]

42. Ozdemir, O.C.; Widener, C.A. Influence of Powder Injection Parameters in High-Pressure Cold Spray. *J. Therm. Spray Technol.* **2017**, *26*, 1411–1422. [CrossRef]
43. Samareh, B.; Stier, O.; Lüthen, V.; Dolatabadi, A. Assessment of CFD Modeling via Flow Visualization in Cold Spray Process. *J. Therm. Spray Technol.* **2009**, *18*, 934–943. [CrossRef]
44. Zabihi Yeganeh, A.; Jadidi, M.; Moreau, C.; Dolatabadi, A. Numerical Modeling of Aerosol Deposition Process. *Surf. Coat. Technol.* **2019**, *370*, 269–287. [CrossRef]
45. Fluent, A. *Ansys Fluent Theory Guide*; ANSYS Inc.: San Diego, CA, USA, 2013.
46. O'Rourke, P.J. Collective Drop Effects on Vaporizing Liquid Sprays. Ph.D. Thesis, Princeton University, Princeton, NJ, USA, 1981.
47. Crowe, C.T.; Schwarzkopf, J.D.; Sommerfeld, M.; Tsuji, Y. *Multiphase Flows with Droplets and Particles*, 2nd ed.; CRC Press: Boca Raton, FL, USA, 2011.
48. Crowe, C.T. Drag Coefficient of Particles in a Rocket Nozzle. *AIAA J.* **1967**, *5*, 1021–1022. [CrossRef]
49. Jadidi, M.; Mousavi, M.; Moghtadernejad, S.; Dolatabadi, A. A Three-Dimensional Analysis of the Suspension Plasma Spray Impinging on a Flat Substrate. *J. Therm. Spray Technol.* **2014**, *24*, 11–23. [CrossRef]
50. Matsufuji, H.; Hasegawa, E. Critical Condition for Collision of Suspended Small Particles with a Body in a Viscous Fluid. *Bull. JSME* **1986**, *29*, 3375–3382. [CrossRef]
51. Phillips, C.G.; Kaye, S.R. The influence of the viscous boundary layer on the critical stokes number for particle impaction near a stagnation point. *J. Aerosol. Sci.* **1999**, *30*, 709–718. [CrossRef]
52. Burwash, W.; Finlay, W.; Matida, E. Deposition of Particles by a Confined Impinging Jet onto a Flat Surface at Re = 10^4. *Aerosol. Sci. Technol.* **2006**, *40*, 147–156. [CrossRef]
53. Bae, G.; Kang, K.; Na, H.; Kim, J.-J.; Lee, C. Effect of Particle Size on the Microstructure and Properties of Kinetic Sprayed Nickel Coatings. *Surf. Coat. Technol.* **2010**, *204*, 3326–3335. [CrossRef]
54. Benim, A.C.; Cagan, M.; Nahavandi, A.; Pasaqualotto, E. RANS Predictions of Turbulent Flow Past a Circular Cylinder over the Critical Regime. In Proceedings of the 5th IASME/WSEAS International Conference on Fluid Mechanics and Aerodynamics, Athens, Greece, 25–27 August 2007.

Disclaimer/Publisher's Note: The statements, opinions and data contained in all publications are solely those of the individual author(s) and contributor(s) and not of MDPI and/or the editor(s). MDPI and/or the editor(s) disclaim responsibility for any injury to people or property resulting from any ideas, methods, instructions or products referred to in the content.